



TECHNISCHE  
UNIVERSITÄT  
WIEN

Vienna University of Technology

D I P L O M A R B E I T

# Determination of the $\Sigma$ - $\pi$ scattering lengths in the weak $\Lambda_c$ decay using Belle data

ausgeführt am

Atominstitut  
der Technischen Universität Wien

und an der  
Österreichischen Akademie der Wissenschaften

unter der Anleitung von  
Privatdoz. Dipl. Ing. Dr. Johann Marton

durch  
Manfred Berger

Goldeggerstraße 70  
3100 St. Pölten

---

Datum

---

Unterschrift



# Note of thanks

I want to thank my supervisor at the Stefan-Meyer Intitute Dr. Johann Marton who made this work possible. Furthermore I thank Dr. Ken Suzuki for his untiring support and the members of the Belle Analysis group at HEPHY, especially Dr. Christoph Schwanda, Dr. Felicitas Breitwick and Robin Glattauer for lending their considerable expertise.



# Abstract

This thesis deals with the analysis of the weak decays of  $\Lambda_c \rightarrow \Sigma\pi\pi$  using Belle data with the ultimate purpose of extracting scattering lengths of  $\Sigma$  and  $\pi$ . The  $\Sigma\pi$  scattering length is one of the important missing experimental inputs to understand the  $\Lambda(1405)$  state, an exotic resonance which can be considered as a quasi-bound state of proton and kaon. A determination of a scattering length of short lived particle is difficult since a direct scattering experiment is not possible. In the case of the  $\Sigma\pi$  system, due to the final state interaction, isospin violation and interference, threshold cusps will appear in the  $\Sigma\pi$  spectra. The strength of the cusp effect reflects the  $\Sigma\pi$  scattering lengths.

The scope of this thesis is limited to the Monte Carlo studies that precede the measurement of real data. The reconstruction of  $\Lambda_c$  in  $\Sigma^+\pi^+\pi^-$ ,  $\Sigma^+\pi^0\pi^0$  and  $\Sigma^0\pi^+\pi^0$  decay modes as well as the determination of branching ratios of those decay modes relative to the reference channel  $pK^-\pi^+$  is presented. Finally the MC  $\Sigma\pi$  spectrum is compared with theoretical predictions.



# Kurzfassung

Diese Diplomarbeit beschäftigt sich mit der Analyse schwacher Zerfälle von  $\Lambda_c \rightarrow \Sigma\pi\pi$  unter Verwendung von Daten des Belle Experiments, mit dem ultimativen Ziel die Streulängen für  $\Sigma$  und  $\pi$  zu extrahieren. Die  $\Sigma\pi$  Streulänge ist eine der wichtigen zum Verständnis des  $\Lambda(1405)$  Zustandes fehlenden experimentalen Größen.  $\Lambda(1405)$  ist eine exotische Resonanz, die als ein quasi gebundener Proton - Kaon Zustand betrachtet werden kann. Die Bestimmung von Streulängen kurzlebiger Partikel ist schwierig da direkte Streuexperimente nicht möglich sind. Im Fall des  $\Sigma\pi$  Systems erscheint ein "threshold cusp" im  $\Sigma\pi$  Spektrum auf Grund von Endzustands Wechselwirkungen, Isospin Verletzung und Interferenz. Die Stärke dieses Effekts reflektiert die Streulänge.

Der Umfang dieser Arbeit ist auf die Monte Carlo Studien, die der Messung realer Daten vorausgehen beschränkt. Die Rekonstruktion von  $\Lambda_c$  in den  $\Sigma^+\pi^+\pi^-$ ,  $\Sigma^+\pi^0\pi^0$  und  $\Sigma^0\pi^+\pi^0$  Zerfallskanälen, sowie die Bestimmung ihrer Verzweigungsverhältnisse relativ zu  $pK^-\pi^+$  ist dargelegt. Das MC  $\Sigma\pi$  Spektrum wird mit theoretischen Vorhersagen verglichen.



# Contents

|          |   |           |
|----------|---|-----------|
| <b>1</b> | <b>Introduction</b>   | <b>10</b> |
| 1.1      | Kaonic nuclear states and $\Lambda(1405)$ . . . . .                   | 10        |
| 1.2      | $\pi\Sigma$ Scattering length . . . . .                               | 11        |
| 1.3      | Experimental determination of $\pi\Sigma$ scattering length . . . . . | 11        |
| 1.3.1    | $\pi\pi$ scattering length and Budini-Fonda-Cabibbo method . . . . .  | 11        |
| 1.3.2    | $\pi\Sigma$ scattering length from $\Lambda_c$ decay . . . . .        | 12        |
| <b>2</b> | <b>The Belle Experiment at KEK</b>                                    | <b>13</b> |
| 2.1      | The KEKB accelerator . . . . .  | 13        |
| 2.2      | The Belle detector . . . . .  | 16        |
| 2.2.1    | Tracking detectors . . . . .  | 17        |
| 2.2.2    | Calorimetry and neutral particles . . . . .                           | 19        |
| 2.2.3    | Particle identification . . . . .                                     | 22        |
| 2.3      | Trigger and data acquisition . . . . .                                | 24        |
| 2.3.1    | Trigger system . . . . .  | 24        |
| 2.3.2    | Data acquisition . . . . .  | 24        |
| 2.3.3    | DST production . . . . .  | 27        |
| 2.4      | Belle data analysis . . . . .   | 27        |
| 2.4.1    | Hadron reconstruction . . . . .                                       | 27        |
| 2.4.2    | Detector simulation . . . . .   | 28        |
| <b>3</b> | <b>Analysis Procedure</b>   | <b>29</b> |
| 3.1      | Data sample . . . . .   | 29        |
| 3.2      | Preselection . . . . .  | 30        |
| 3.3      | BDT and Input variables . . . . .                                     | 31        |
| 3.4      | Background . . . . .  | 44        |
| 3.5      | Yield extraction . . . . .  | 49        |
| 3.6      | Systematic Uncertainties . . . . .                                    | 60        |

|          |                                     |           |
|----------|-------------------------------------|-----------|
| 3.7      | Branching ratios . . . . .          | 63        |
| 3.8      | $\Sigma\pi$ mass spectrum . . . . . | 63        |
| <b>4</b> | <b>Conclusion and Outlook</b>       | <b>66</b> |
| <b>5</b> | <b>Apendix</b>                      | <b>67</b> |
| 5.1      | Tables of fit parameters . . . . .  | 67        |
|          | <b>Bibliography</b>                 | <b>73</b> |

# Chapter 1

## Introduction

### 1.1 Kaonic nuclear states and $\Lambda(1405)$

The  $\bar{K}N$  interaction near and below threshold is predicted to be attractive [1, 2, 3], which leads to a prediction of an existence of  $K^-$  bound states in nuclei [1, 4, 5, 6]. The results of experimental searches [7, 8, 9, 10, 11] are mixed. An interpretation of the resonance structures beyond its baryon number 2 and strangeness  $-1$  is dispersed, leaving still open room for discussion of the existence of a  $K^-pp$  state. An important ingredient for a theoretical description of such kaonic bound states is the subthreshold  $\bar{K}N$  scattering amplitudes. Experimental constraints are given mostly at or above the threshold [12, 13], therefore, the subthreshold behaviour of  $\bar{K}N$  amplitude, which is essential for the kaonic nuclear states, needs to rely on a model dependent extrapolation with sizable uncertainty [2, 3, 14].

The subthreshold behaviour of  $\bar{K}N$  scattering is also important to understand the  $\Lambda(1405)$  resonance state [14, 15].  $\Lambda(1405)$  is known to be difficult to be described with an ordinary three-quark picture in the constituent quark model, hence it is one of the oldest exotic hadrons [16]. It is by now widely believed that  $\Lambda(1405)$  is a quasi-bound state of  $\bar{K}N$  [14, 15, 17]. The  $\Lambda(1405)$  resonance is located below the  $\bar{K}N$  threshold and is embedded in the  $\pi\Sigma$  continuum in coupled-channel meson-baryon scattering models.

Chirally motivated models [18, 15] envisage the so-called two-pole structure of  $\Lambda(1405)$ , namely that the nominal  $\Lambda(1405)$  is a superposition of two pole states, one at around 1420 MeV with a narrower width and dominantly attributed to  $\bar{K}N$  state, the other at around 1390 MeV with a broader width, dominantly attributed to  $\pi\Sigma$  state. The higher and hence shallower pole is more relevant to the kaonic systems. Therefore, whether a  $\bar{K}N$  interaction used for a few-body calculation is based on this

hypothesis or not has a decisive influence in predicting binding energies and widths of the  $K^-$  few body nuclear systems [6].

## 1.2 $\pi\Sigma$ Scattering length

While the position of the higher pole has no strong model dependence because of the experimental constraints from  $K^-p$  scattering and kaonic hydrogen data, the position and the width of the lower pole has large model dependence due to the lack of  $\pi\Sigma$  scattering length information. Positive experimental claims of an observation of  $\bar{K}NN$  state as currently available are similarly indicating a large binding energy of 100 MeV [7, 8, 11]. This is where the  $\pi\Sigma$  threshold is located, at 100 MeV below the  $\bar{K}N$  threshold. Therefore an understanding of the coupling of  $\bar{K}N$  to  $\pi\Sigma$  channel is essential for an understanding of those experimental observation of a strange dibaryon.

There's no experimental data available on the  $\pi\Sigma$  scattering length at this moment. Any constraint to it will improve our understanding of  $\Lambda(1405)$  and the kaonic nuclear states.

## 1.3 Experimental determination of $\pi\Sigma$ scattering length

An experimental evaluation of scattering lengths of short lived particles faces a trivial difficulty since a scattering experiment is extremely difficult. Amongst the  $\pi\pi$  scattering length is the most studied one because of its importance as well as its attainability. See a recent review on the history of pion-pion scattering [19].

### 1.3.1 $\pi\pi$ scattering length and Budini-Fonda-Cabibbo method

One of the ideas for avoiding this difficulty is to make use of a final-state-interaction (FSI). Budding and Fondain pointed out in 1961 [20] that a  $\pi\pi$  scattering length can be measured as a threshold cusp effect in the  $\pi^0\pi^0$  partial invariant mass spectrum of  $K \rightarrow \pi^+\pi^0\pi^0$  decay because of isospin violation, charge-exchange rescattering and amplitude interference. The idea, however, had been forgotten due to lack of sufficient  $K \rightarrow 3\pi$  data which enabled this analysis, till N. Cabibbo reinvent the same idea in 2004 [21]. This idea was successfully applied to the high statistics data of NA48/2, the  $K \rightarrow \pi^+\pi^0\pi^0$  decay [22, 23]. 60M samples of  $K^\pm \rightarrow \pi^\pm\pi^0\pi^0$  lead to the most precise determination of  $a_0 - a_2$  as well as  $a_0$  and  $a_2$  to date [23].

### 1.3.2 $\pi\Sigma$ scattering length from $\Lambda_c$ decay

Recently the Budini-Fonda-Cabibbo method has been extended [24] to the  $\Sigma\pi$  system using the weak  $\Lambda_c(2286) \rightarrow \Sigma\pi\pi$  decay. Requiring a sufficiently large mass differences ( $>5$  MeV) between  $\Sigma\pi$  systems before and after the rescattering in order the cusp structure to experimentally be detectable, the following rescattering modes,  $\pi^+\Sigma^- \rightarrow \pi^-\Sigma^+$ ,  $\pi^+\Sigma^- \rightarrow \pi^0\Sigma^0$  for  $(\pi\Sigma)^0$  mode and  $\pi^+\Sigma^0 \rightarrow \pi^0\Sigma^+$  for  $(\pi\Sigma)^+$  mode are of interest.

Hence the following  $\Lambda_c \rightarrow \Sigma\pi\pi$  decays are studied.

$$\Lambda_c \rightarrow \Sigma^+\pi^+\pi^- \quad (3.6 \pm 1.0\%) \quad (1.1)$$

$$\Lambda_c \rightarrow \Sigma^+\pi^0\pi^0 \quad (n.A.) \quad (1.2)$$

$$\Lambda_c \rightarrow \Sigma^0\pi^+\pi^0 \quad (1.8 \pm 0.8\%) \quad (1.3)$$

The number in brackets is the branching ratio as given by the Particle Data Group [25]. The branching ratio of  $\pi^0\pi^0$  mode is so far not known, probably because of an experimental difficulty to reconstruct this channel as the final state includes 3  $\pi^0$ s, in other words, 6 gamma rays. The branching ratio, however, would be about the same order as the  $\pi^+\pi^0$  mode from an isospin consideration. Two constraints could be given to three different isospin components of  $\pi\Sigma$  scattering lengths. The  $I = 2$  component of the scattering length might needed to be determined by the lattice QCD.

# Chapter 2

## The Belle Experiment at KEK

Belle denotes both the  $B$  factory at the Japanese national accelerator laboratory KEK and the international collaboration that built and operated the detector and is still analyzing its experimental data. It consists of the asymmetric energy  $e^+e^-$  collider KEKB and the Belle apparatus located in the single interaction region of the machine. Data taking took place in the years 1999 to 2010.

### 2.1 The KEKB accelerator

For a detailed description of the KEKB collider see Ref. [33]. The following sections follow closely the description in ref. [26]. KEKB is a two ring energy-asymmetric electron positron collider (Fig. 2.1) consisting of two storage rings with a circumference of about 3 km. A 8 GeV electron ring (High Energy Ring, HER) and a 3.5 GeV positron ring (Low Energy Ring, LER), which intersect at the location of the Belle detector.

The beams collide with a finite crossing angle of 22 mrad. The center-of-mass (c.m.) energy of the collisions is given as follows,

$$\sqrt{s} = \sqrt{(p_{\text{LER}} + p_{\text{HER}})^2} \approx 2\sqrt{E_{\text{LER}}E_{\text{HER}}} \approx 10.58 \text{ GeV} , \quad (2.1)$$

with  $p_{\text{LER}}$  and  $p_{\text{HER}}$  denoting the 4-momenta of the colliding beam particles, and  $E_{\text{LER}}$  and  $E_{\text{HER}}$  their energies. This is the energy of the  $\Upsilon(4S)$  resonance which decays almost exclusively to a pair of  $B$  mesons (either  $B^+B^-$  or  $B^0\bar{B}^0$ ) [27]. Electron-positron collisions proceeding through the  $\Upsilon(4S)$  state will thus lead to events containing two  $B$  mesons without any additional particles. The energy asymmetry of

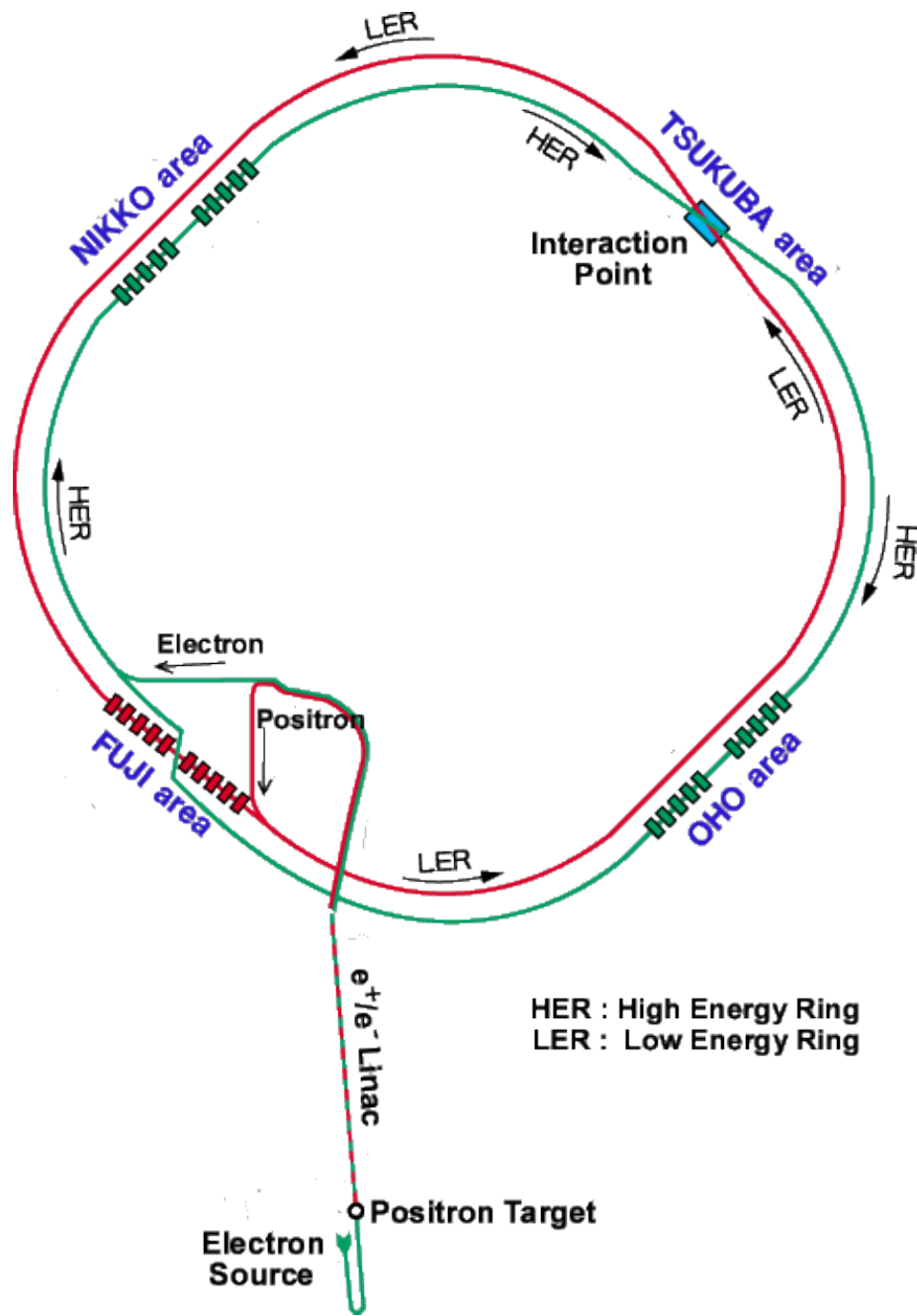


Figure 2.1: The layout of KEKB.

Table 2.1: Cross sections and event rates of various processes in  $e^+e^-$  collisions at  $\sqrt{s} = 10.58$  GeV (1 nb=  $10^{-33}$  cm<sup>2</sup>). QED refers to Bhabha and radiative Bhabha processes. The event rates are calculated at the nominal instantaneous KEKB luminosity of  $10^{34}$  cm<sup>-2</sup>s<sup>-1</sup>.

| Process  | $\sigma$ (nb) | Rate (Hz) |
|--|---------------|-----------|
| $e^+e^- \rightarrow \Upsilon(4S) \rightarrow B\bar{B}$ | 1.1           | 11        |
| $e^+e^- \rightarrow q\bar{q}$ ( $q = u, d, s, c$ )     | 3.3           | 33        |
| $e^+e^- \rightarrow \tau^+\tau^-$                      | 0.93          | 9         |
| QED ( $25.551^\circ < \theta < 159.94^\circ$ )         | 37.8          | 378       |
| $\gamma\gamma \rightarrow q\bar{q}$ ( $w > 500$ MeV)   | 11.1          | 111       |

the colliding beams leads to the  $\Upsilon(4S)$  events being boosted

$$\beta\gamma \approx \frac{E_{\text{HER}} - E_{\text{LER}}}{M_{\Upsilon(4S)}} \approx 0.425 \quad (2.2)$$

with respect to the laboratory frame The c.m. system thus moves along the positive  $z$  direction<sup>1</sup>. As the produced  $B$  meson are nearly at rest in the c.m. frame, the boost allows a measurement of the decay time different from the spatial separation of the  $B$  decay vertices. This time distribution  $\Delta t$  is required for observing mixing-induced  $CP$  violation at Belle.

The number of events produced at KEKB through a process with the cross section  $\sigma$  (Table 2.1) is given by the product  $\sigma\mathcal{L}$ , where  $\mathcal{L}$  is the integrated luminosity delivered by KEKB. Statistical uncertainty of measurements generally decreases with  $1/\sqrt{\mathcal{L}}$ . This makes the integrated luminosity delivered by KEKB the most important parameter for the experiment.

The instantaneous luminosity of KEKB was designed as  $10^{34}$  cm<sup>-2</sup>s<sup>-1</sup> but much higher values (up to  $2.11 \times 10^{34}$  cm<sup>-2</sup>s<sup>-1</sup> on June 17, 2009) have been reached. However, this still only corresponds to a production rate for  $e^+e^- \rightarrow \Upsilon(4S) \rightarrow B\bar{B}$  process of about 20 Hz only. The time development of the integrated KEKB luminosity is shown in Fig. 2.2. The final value delivered by KEKB is  $1040$  fb<sup>-1</sup>

<sup>1</sup>The Belle coordinate system is defined as follows: The  $z$ -axis is aligned with the LER beam but is opposite to the positron momentum, the  $y$ -axis is vertical, and the  $x$ -axis is horizontal and points to the outside of the ring.

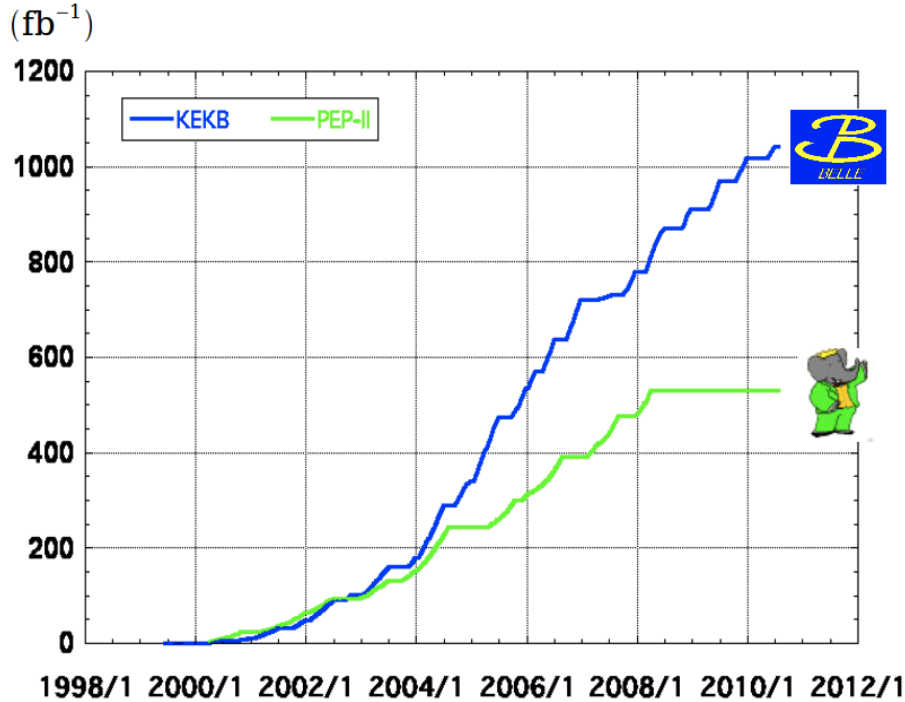


Figure 2.2: History of the integrated luminosity of KEKB, compared to the performance of PEP-II, which delivered  $B\bar{B}$  pairs to the BaBar experiment.

( $1 \text{ b}^{-1} = 10^{24} \text{ cm}^{-2}$ ). About  $711 \text{ fb}^{-1}$  were recorded on the  $\Upsilon(4S)$  resonance, corresponding to 772 million  $B\bar{B}$  events.  $87 \text{ fb}^{-1}$  were taken below the resonance for background measurements. The remaining data were taken at other energies. Belle's  $B\bar{B}$  sample is about twice as large as the one recorded by the BaBar experiment in California.

## 2.2 The Belle detector

The Belle detector itself (Fig. 2.3) is a large-solid-angle magnetic spectrometer that determines the number of charged and neutral particles produced in the  $e^+e^-$  collisions, measures their momentum and energy, and assigns a mass hypothesis (pion, kaon, ...). This is achieved using several sub-detectors which are described starting from the innermost. Most of the sub-detectors are located within the 1.5 T magnetic

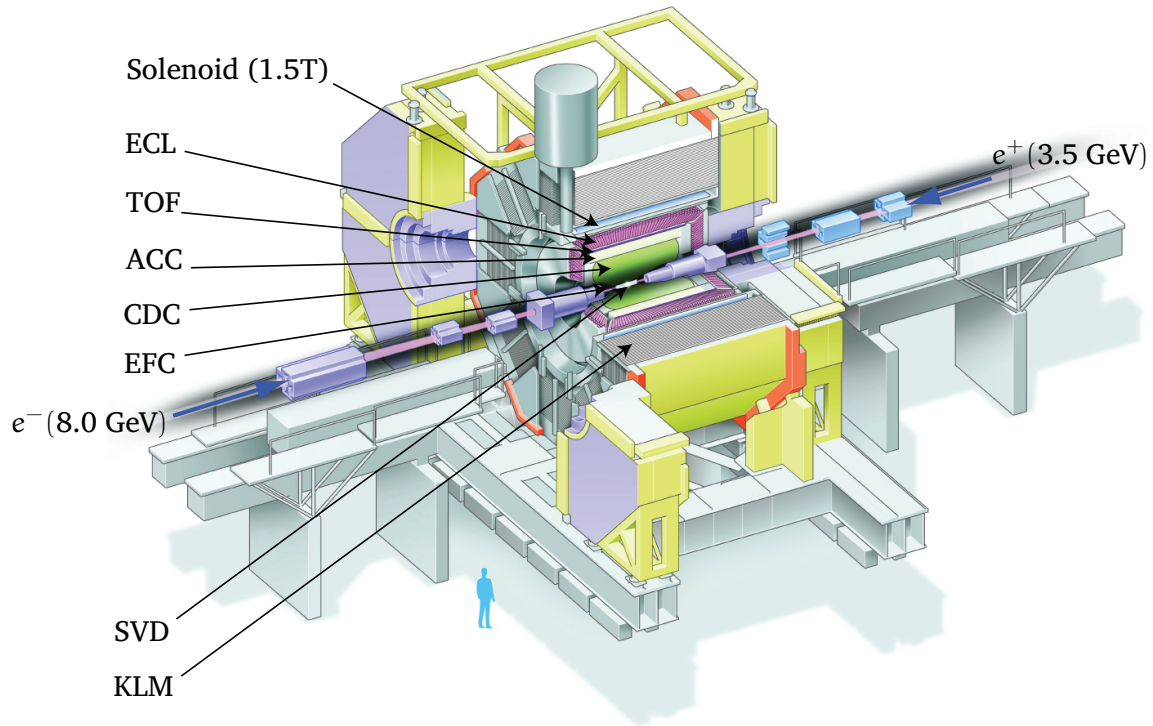


Figure 2.3: Schematic view of the Belle detector.

field of the superconducting coil at  $R = 170 \text{ cm}$ .<sup>2</sup> The purpose of this field is to constrain charged particles to helical trajectories, so that their momentum can be inferred from the track curvature. A more detailed review of the Belle spectrometer can be found in Ref. [34].

### 2.2.1 Tracking detectors

Tracking, the reconstruction of charged particle trajectories, is accomplished by two sub-detectors completely within the 1.5 T magnetic field of the solenoid: the Silicon Vertex Detector (SVD) and the Central Drift Chamber (CDC).

---

<sup>2</sup>Spherical coordinates in the Belle frame are introduced as follows: The radial distance is defined by  $R = \sqrt{x^2 + y^2}$ ,  $\theta$  is the polar angle with respect to the  $z$ -axis,  $\phi$  is the azimuthal angle with respect to the  $x$ -axis.

## SVD

Located on the beryllium beam pipe the SVD consists of double-sided silicon strip detectors (DSSDs) and measures charged particles in the vicinity of the  $e^+e^-$  interaction point. DSSDs are semiconductor diodes ( $p$ - $n$  junction) operated in reverse bias. The passage of a charged particle through the depletion region creates electron-hole pairs. These charges drift to strips located on both the  $p$ - and  $n$ -sides of the sensor. Using the electrical signals induced at these strips, the intersection point of the track with the sensor can be determined with an accuracy of a few tens of micrometer. The strips on the  $p$ -side are aligned along the beam axis and thus measure the azimuthal angle  $\phi$ . The  $n$ -strips are perpendicular to the beam axis and measure  $z$ . At Belle, each DSSD has 1280 sense strips and 640 readout pads on opposite sides. The strip distance is  $42\ \mu\text{m}$  in  $z$ -direction and  $25\ \mu\text{m}$  in  $\phi$ . The overall DSSD size is  $57.5 \times 33.5\ \text{mm}^2$ .

Physically the DSSDs are arranged in one-dimensional structures called ladders. These ladders form a layer around the beam pipe. Two different SVD configurations have been used: SVD1 with three concentric layers from 1999 to July 2003 (Fig. 2.4), and SVD2 with four layers, from October 2003 to 2010. The polar angle coverage of SVD1 is  $23^\circ < \theta < 139^\circ$ . SVD2 extends this to  $17^\circ < \theta < 150^\circ$ .

## CDC

The chamber has 50 cylindrical layers of anode sense wires and three cathode strip layers. The wire arrangement is either axial or slightly tilted to allow measurement of the  $z$ -position. The Central Drift Chamber is shown in Fig. 2.5. The wires are located between  $R = 8.3\ \text{cm}$  and  $R = 86.3\ \text{cm}$ . The chamber is asymmetric in the  $z$ -direction with the same polar angle coverage as the SVD2:  $17^\circ < \theta < 150^\circ$ . The CDC filling gas is a 50% helium-50% ethane mixture.

A charged particle traveling through the chamber ionizes the counting gas with the produced electrons drifting to the wires. The field is strongest in the direct vicinity of the wires so that primary charges are amplified. Through this amplification an electric signal can be recorded on the respective wire. Using wire position and drift time, the intersection point of the particle trajectory with the wire can be measured up to a  $100\ \mu\text{m}$  precision.

## Operation

Charged particle trajectories measured in the CDC together with SVD hit points allow for a precise determination of decay vertex positions. The relative precision

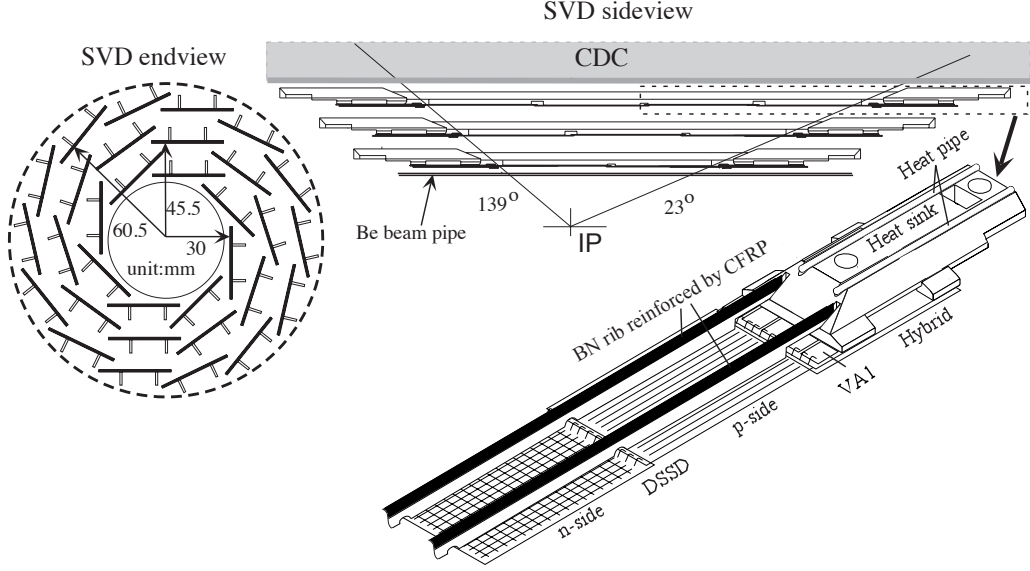


Figure 2.4: Configuration of the first version of the vertex detector (SVD1) shown in a cross-section (left) and in a side view (right).

obtained for the transverse particle  $\vec{p}_T$  momentum, defined as is the projection of the 3-momentum  $\vec{p}$  into the  $xy$  plane, is  $(0.3 \times \sqrt{p_T^2 + 1})\%$ . The distance of closest approach of the particle track to the interaction point is called impact parameter. Resolution for these parameters are  $\sigma_{xy} = 19 \oplus 50/(p\beta \sin^{3/2} \theta) \mu\text{m}$  and  $\sigma_z = 36 \oplus 42/(p\beta \sin^{5/2} \theta) \mu\text{m}$ , the symbol  $\oplus$  denoting quadratic addition the error components.

## 2.2.2 Calorimetry and neutral particles

The electromagnetic calorimeters (ECL) purpose is the measurement of photons. Belle has no system to fully measure long-lived neutral hadrons, such as  $K_L$  particles. The extreme forward calorimeter (EFC) is only used as an online luminosity monitor.

### ECL

The ECL is composed of 8736 tower-shaped CsI(Tl) crystals, arranged as shown in Fig. 2.6. The ECL is separated into three parts: the forward endcap ( $12.4^\circ < \theta < 31.4^\circ$ ), the barrel ( $32.2^\circ < \theta < 128.7^\circ$ ) and the backward endcap ( $130.7^\circ < \theta < 155.1^\circ$ ). The barrel region is 3.0 m long with an inner radius of 1.25 m. The

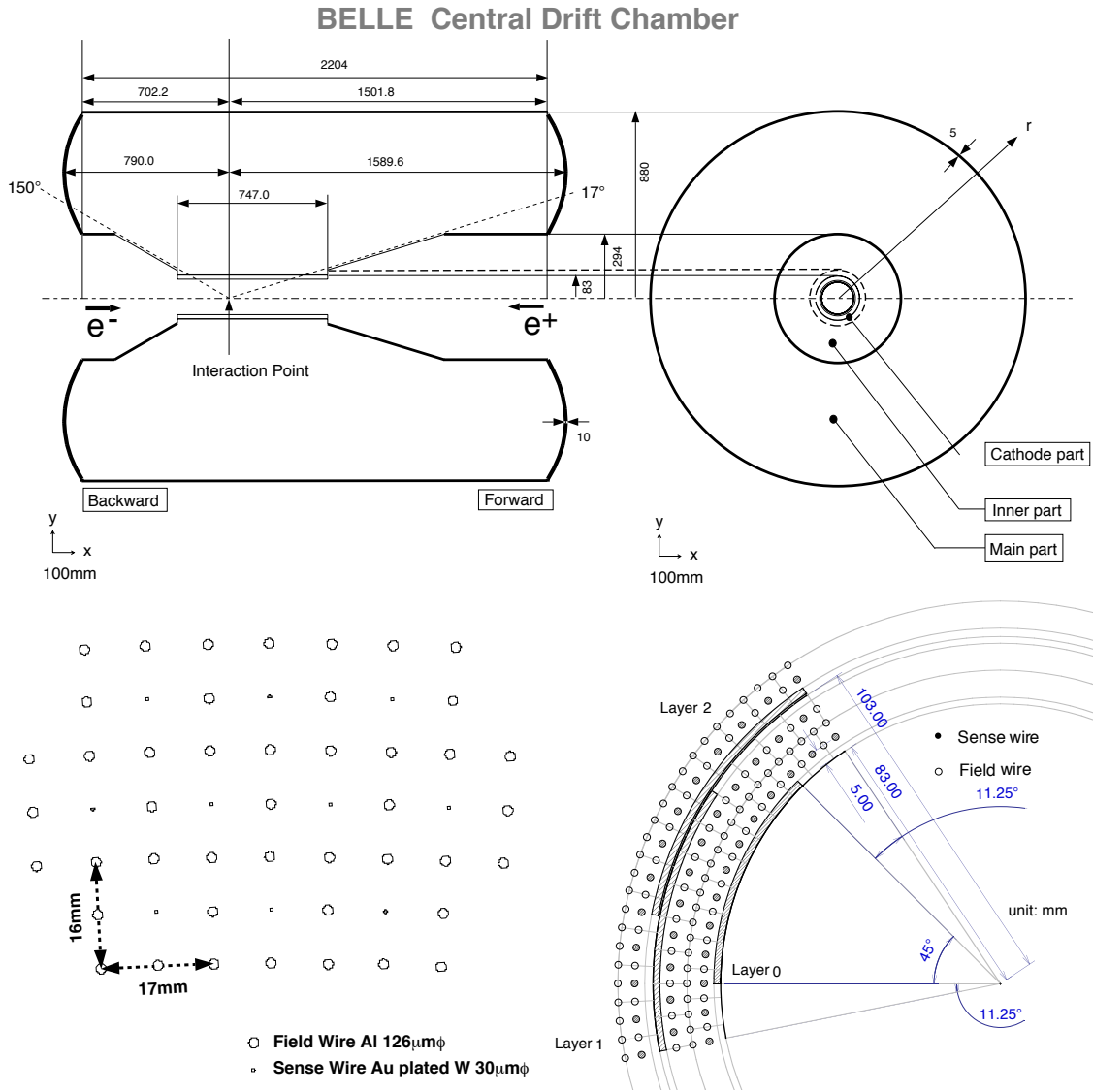


Figure 2.5: Overview of the CDC structure (top) and CDC wire configuration (bottom).

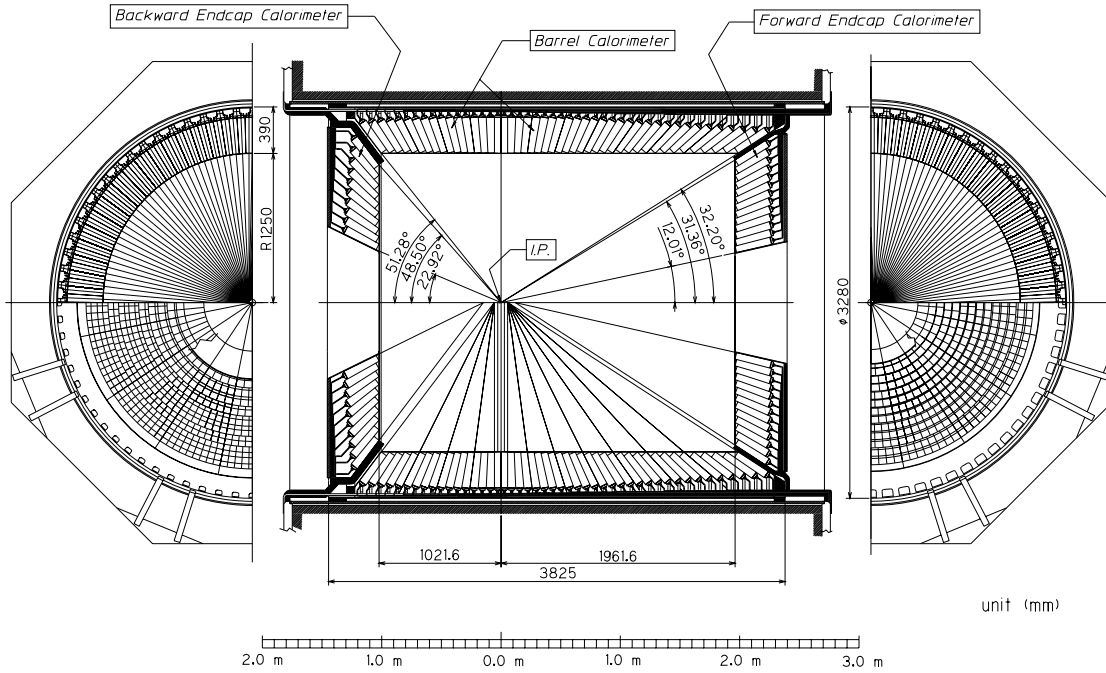


Figure 2.6: Configuration of the ECL.

endcaps are located at  $z = 2.0$  m and  $z = -1.0$  m. A photon hit in a crystal initiates an electromagnetic shower and is stopped completely, as the 30 cm height of the crystals corresponds to 16.2 radiation lengths  $X_0$ . The scintillation light generated is proportional to the deposited energy and collected by a pair of photodiodes.

The position resolution of a photon with energy  $E$  is about  $\sigma_{\text{pos}} = 0.5 \text{ cm}/\sqrt{E}$  ( $E$  in GeV). The relative energy resolution obtained with the ECL is  $\sigma_E/E = 1.3\%/E$  ( $E$  in GeV).

## KLM

The KLM exclusively detects  $K_L$  and muons, hence the name. It has no bearing on the analysis presented here.

### 2.2.3 Particle identification

Only the following charged particles are long lived enough to be seen by the Belle detector: electrons, muons, pions, kaons and protons. Determining which of these mass hypothesis to assign to a track is the task of Particle identification. Pions are by far the most common with a share of about 80%.

#### Hadron identification

The identification of pions, kaons and protons uses these three nearly independent measurements:

- the energy loss measurement  $dE/dx$  by the CDC,
- the Cherenkov light yield observed in the ACC, and
- the time-of-flight measurement by the TOF.

The CDC supplies charged track points and information on energy loss in its detector medium. The latter allows to separate pions and kaons at the level of  $3\sigma$  for momenta between 0.4 and 0.6 GeV/ $c$  (Fig. 2.7).

The aerogel Cherenkov counter (ACC) extends the particle identification system to high momenta and is an array of threshold counters located outside of the CDC. Its basic operation is based on the emittance of Cherenkov light when a particle with velocity greater than the speed of light in medium passes through. Through the choice of refractive indices of the ACC only pions in the momentum range of 1 to 4 GeV/ $c$  produce Cherenkov light while kaons or protons do not.

The time-of-flight (TOF) system consists of 128 plastic scintillation counters located between the ACC and the ECL and read out by fine-mesh photo-multiplier tubes. The achieved time resolution is about 100 ps. Located 1.2 m from the interaction point, the TOF can distinguish the arrival times of pions and kaons below a momentum of about 1.2 GeV/ $c$ , which encompasses 90% of the particles produced in  $\Upsilon(4S)$  decays.

A likelihood function for each of these three inputs is calculated. The overall likelihood of being a pion or kaon is derived by multiplying the three functions. Kaons in the momentum range from 0.5 to 4 GeV/ $c$  are selected with an efficiency of about 90% and a pion fake rate, defined as the probability to misidentify a pion as a kaon, of a few percent.

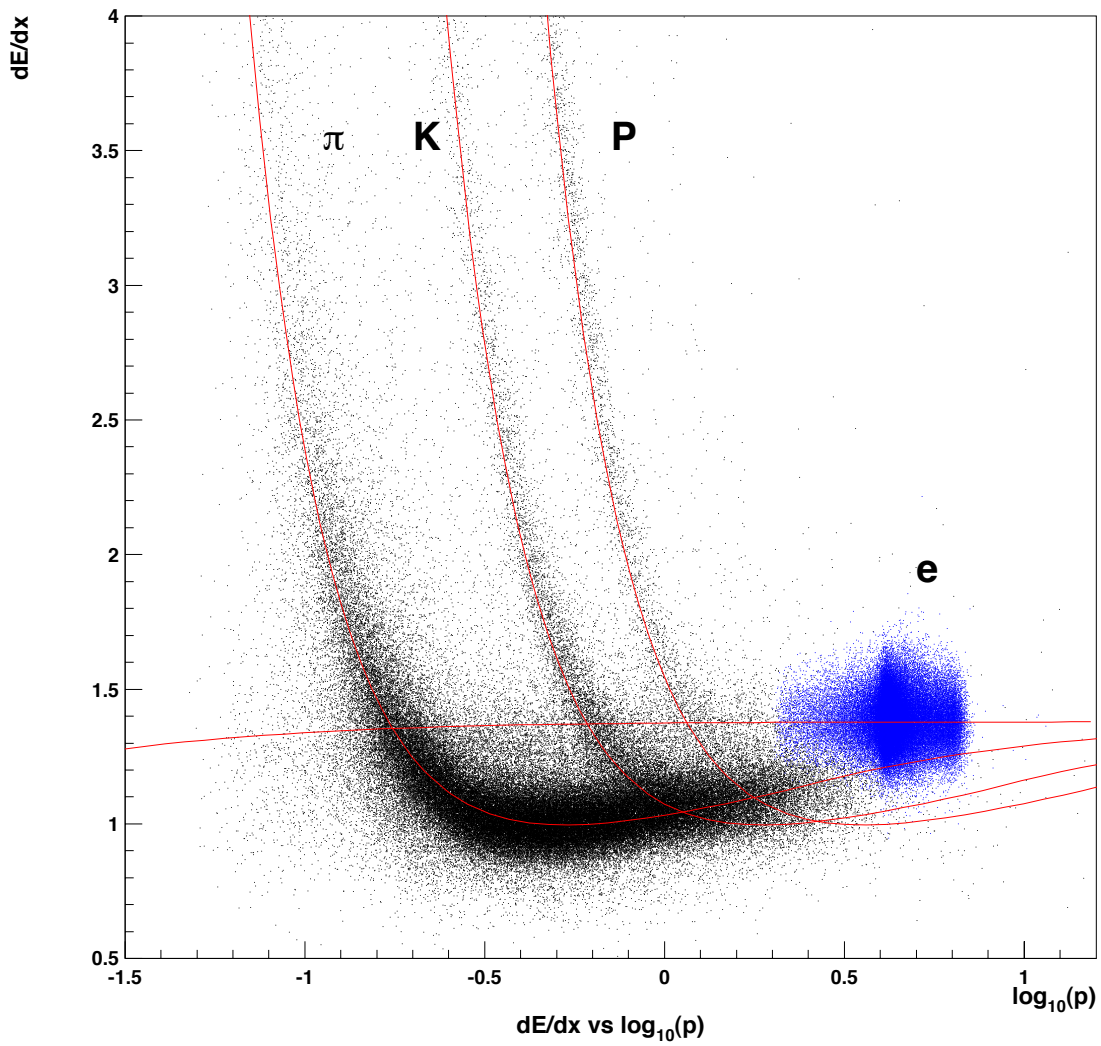


Figure 2.7: Particle type separation with the energy loss measurement  $dE/dx$  in the CDC.

## 2.3 Trigger and data acquisition

### 2.3.1 Trigger system

The rate of collision for bunches of electrons and positrons at KEKB can occur with the beam crossing rate of 509 MHz, that is every two nanoseconds. Interesting events however happen only at several Hz. The cross-sections for events like  $e^+e^- \rightarrow \Upsilon(4S) \rightarrow B\bar{B}$ ,  $e^+e^- \rightarrow q\bar{q}$  or  $e^+e^- \rightarrow \tau^+\tau^-$  lie in the nanobarn range (Table 2.1). The purpose of the trigger system is to exclude uninteresting events with large cross-section (such as, *e.g.*, Bhabha scattering,  $e^+e^- \rightarrow e^+e^-$ ) and other backgrounds from data acquisition. Examples for the latter would be residual beam, gas interactions, synchrotron radiation and cosmic rays. The trigger conditions have to be strict enough to always keep the rate within tolerance, in this case below 500 Hz, while also exhibiting high efficiency for physics events.

The Belle trigger system consists of the Level-1 hardware trigger and the Level-3 and Level-4 software filters. The Level-1 includes the sub-detector trigger systems and the so called Global Decision Logic (GDL), the central trigger system called shown in Fig. 2.8. The first are sensitive to both charged tracks and energy deposits which is essential for stable Level-1 operation. The time scales involved in the GDL operation are about  $1.85 \mu\text{s}$  for receiving all trigger signals and  $2.2 \mu\text{s}$  for issuing its decision. Only after a positive Level-1 does the readout start.

The combined efficiency of the trigger system for hadronic events is more than 99.5%.

### 2.3.2 Data acquisition

Data Acquisition system (DAQ) collects sub-detector information as shown in Fig. 2.9. The event builder combines data from the seven partitions handling one sub-detector each. The event output is transferred to an online computer farm, where Level-3 filtering takes place. From here data are sent to a mass storage system.

The CDC, ACC, TOF, ECL and EFC detectors are read out using the charge-to-time ( $Q$ -to- $T$ ) technique: The charge is stored in a capacitor and discharged at a constant rate with two pulses, corresponding to the start and stop times. The SVD readout uses a different system, as advanced signal processing (data sparsification) is required.

The typical size of a hadronic event ( $e^+e^- \rightarrow q\bar{q}$ ,  $e^+e^- \rightarrow \Upsilon(4S) \rightarrow B\bar{B}$ ) is about 30 kByte, which corresponds to a maximum data transfer rate of 15 MByte/s.

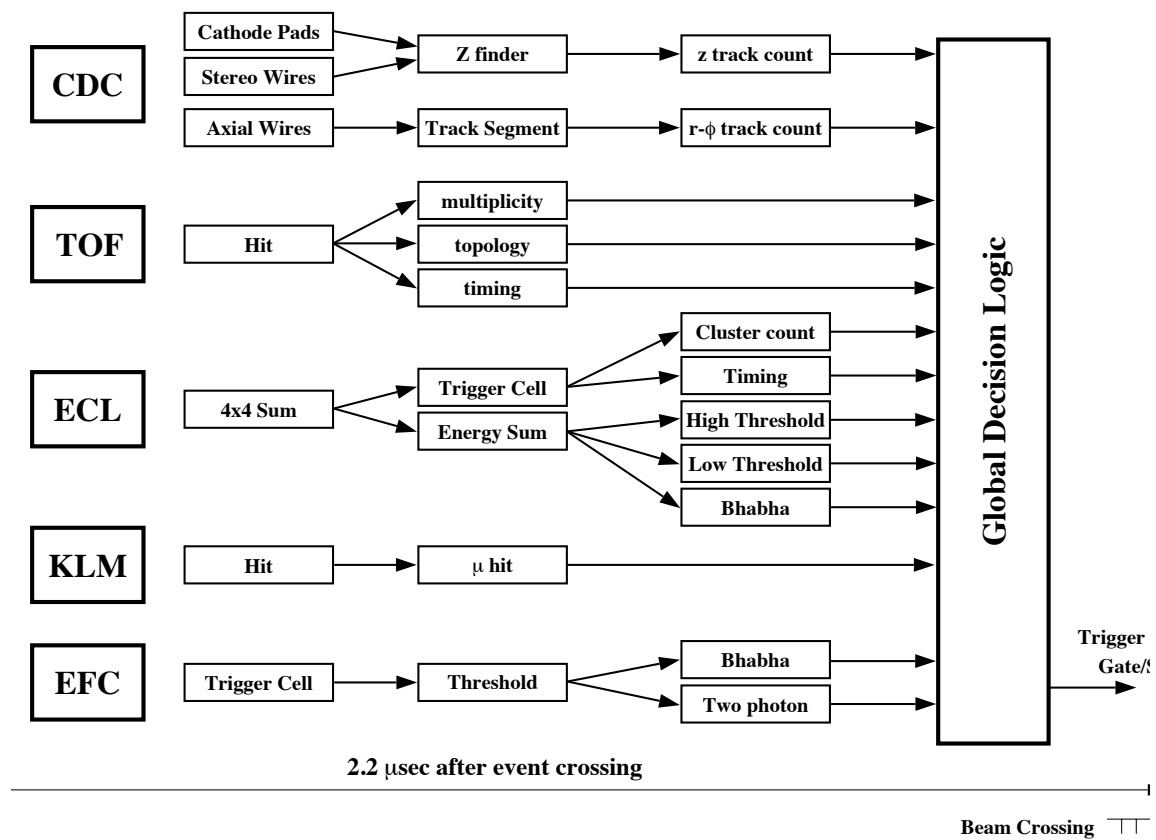


Figure 2.8: The Level-1 trigger system of the Belle detector.

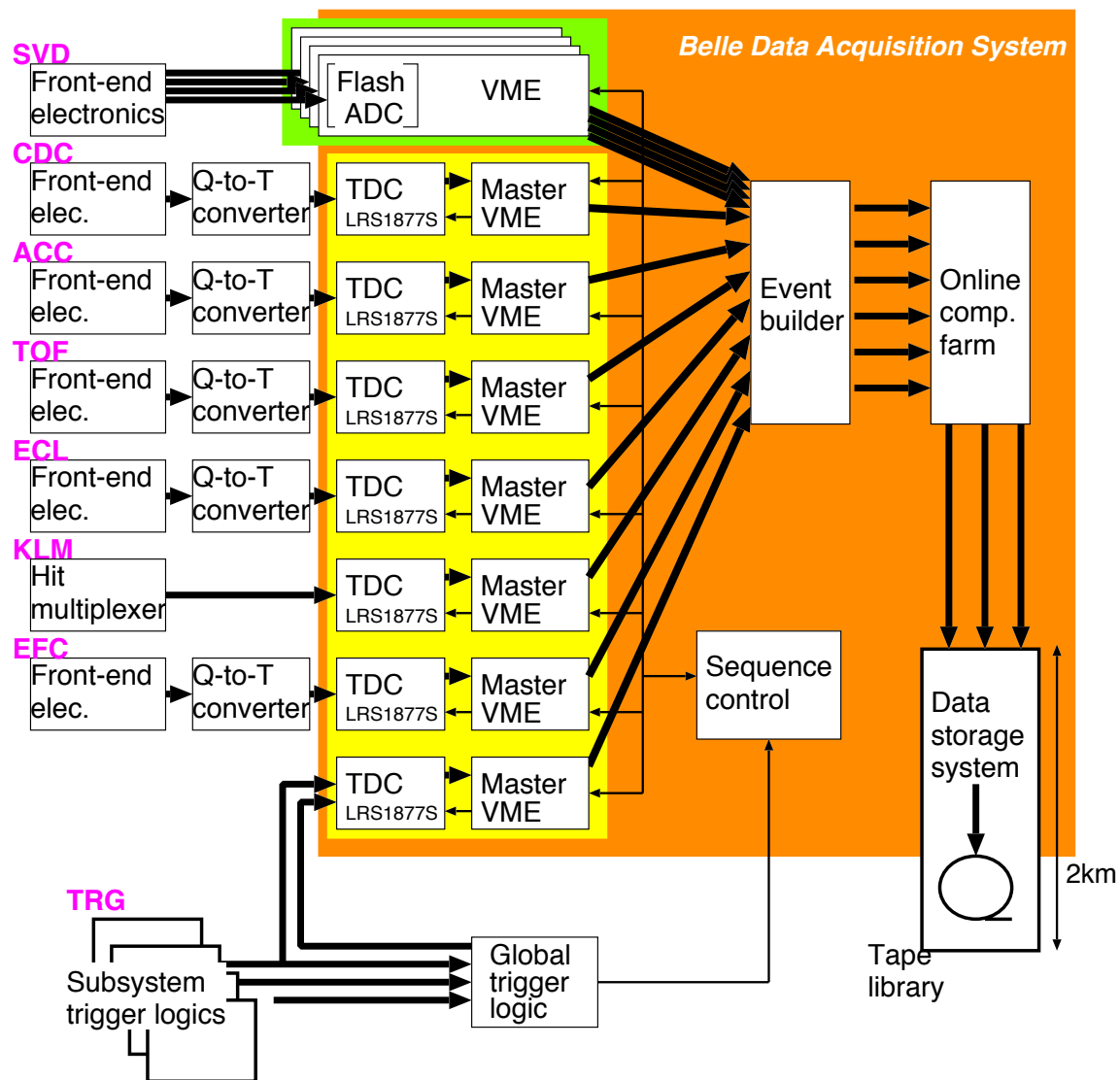


Figure 2.9: Overview of the Belle data acquisition system.

### 2.3.3 DST production

In the final stage, the number of events is further reduced by the Level-4 filter. Accepted events are reconstructed and stored in so-called DST (Data Summary Tape) files. Only now are detector signals converted to physical properties like 4-vectors. Finally events are assigned to different streams (so-called skims). The stream relevant to most Belle physics analyses is called HadronB(J) and contains hadronic events (mainly  $e^+e^- \rightarrow \Upsilon(4S) \rightarrow B\bar{B}$ ,  $e^+e^- \rightarrow q\bar{q}$  and  $e^+e^- \rightarrow \tau^+\tau^-$ ). A hadronic event at this level is about 40 kByte. Access by the end-user only occurs after one further step of reorganisation, producing MDST (mini -DST) files. These contain all records of a certain type *e.g.* `mdst_Vee2` contains all candidates for neutral particles reconstructed from two charged tracks. Every daughter particle is linked by a unique index to `mdst_charged` which contains all recorded charged tracks. Similarly `mdst_Pi0` is filled with all  $\gamma\gamma$  combinations that suffice a  $\pi^0$  mass hypothesis.

## 2.4 Belle data analysis

### 2.4.1 Hadron reconstruction

Most physics analyses at Belle involve the reconstruction of  $B$  mesons (either  $B^0$  or  $B^+$ , produced in  $e^+e^- \rightarrow \Upsilon(4S) \rightarrow B\bar{B}$  collision events in almost equal amounts [27]), although the analysis presented here focuses on  $e^+e^- \rightarrow c\bar{c}$ .  $B$  mesons travel about 200  $\mu\text{m}$  before decaying, and most of their decay products also decay before reaching the first active surface of the detector at 2 cm from the interaction point (IP). The same is true for most hadrons. Only five types of charged particles (electrons, muons, charged pions and kaons, and protons), photons and long-lived neutral particles such as  $K_S^0$ ,  $K_L^0$ ,  $\Lambda^0$ , or neutrons survive long enough to reach active surfaces. There are usually about ten neutral and ten charged particles in a hadronic event. About 80% of the latter are pions.

To reconstruct, *e.g.*, the decay  $B^- \rightarrow D^0\pi^-$  followed by  $D^0 \rightarrow K^-\pi^+$  in hadronic events, first all combinations of oppositely charged kaons and pions in the event are tried. Then the invariant mass of the  $K\pi$  pair defined as

$$m_{K\pi} = |p_K + p_\pi| = \sqrt{(E_K + E_\pi)^2 - (\vec{p}_K + \vec{p}_\pi)^2} . \quad (2.3)$$

is calculated.  $p_K = (E_K, \vec{p}_K)$  and  $p_\pi = (E_\pi, \vec{p}_\pi)$  are the 4-momenta of the kaon and pion candidates, as determined by the tracking system. Combinations selected in a window around the  $D^0$  mass are retained for further analysis. These  $D^0$  candidates

are then combined with a different pion in the event to form charged  $B$  meson candidates.

For  $B$  - mesons the distinct signal shape, spherical compared to jet - like for lighter quarks and tagging are valuable tools for improving signal purity. The main tool for events from the  $e^+e^- \rightarrow c\bar{c}$  continuum are stricter kinetic requirements.

## 2.4.2 Detector simulation

An important tool of data analysis is Monte Carlo (MC) simulation. Simulated events are identical to real data events with the only but important difference that the underlying physics process is entirely known. Typically Belle uses MC studies for

- determination of the reconstruction efficiency of the entire analysis chain,
- estimation of the amount of background events passing the selection criteria,
- optimization and validation of the whole analysis procedure.

Simulation follows several steps. Physics processes and decays of short lived particles are simulated in the event generator. In Belle, the EvtGen generator [35] is used for  $\Upsilon(4S) \rightarrow B\bar{B}$  and  $e^+e^- \rightarrow q\bar{q}$  ( $q = u, d, s, c$ ) collision events. The charged and neutral particles produced are followed through the entire Belle detector using the GEANT3 package [36]. Here all secondary processes and interactions in the detector material are simulated. In conclusion the MC generated data is saved in the same DST format as real measurements.

Usually two types of MC are differentiated: MC only containing the decay mode or physics process studied is called signal MC and usually created by the user. Generic MC is produced by the collaboration and aims to include all background processes. At least three times the real data luminosity are available for  $\Upsilon(4S) \rightarrow B\bar{B}$  and  $e^+e^- \rightarrow q\bar{q}$  ( $q = u, d, s, c$ ) events as generic MC samples.

# Chapter 3

## Analysis Procedure

The policy of the Belle collaboration is that every analysis has to be performed blind on MC data first and only after an internal review process is positive can real data be used. This section describes the reconstruction and optimization of the selection criteria for  $\Lambda_c$  in the three  $\Sigma\pi\pi$  modes under investigation, as well as of the reference channel  $pK^-\pi^+$ . The preselection is described in section 3.2. Optimization is performed using Boosted Decision Trees (BDT) via maximisation of a Figure of Merit (FoM) defined as  $S/\sqrt{S+B}$  in section 3.3, the parametrization for the Probability density functions used for yield extraction is found in 3.5, a first list of contributions to the systematic error on the relative branching ratios is presented in 3.6 and a MC spectrum of the  $\Sigma^+\pi^-$  invariant mass compared with theoretical predictions is presented in section 3.7.

### 3.1 Data sample

The analysis is performed using  $703 \text{ fb}^{-1}$  of HadronB data collected at the  $Y(4S)$  resonance with the Belle detector at the KEKB asymmetric energy  $e^+e^-$  collider.

For determination of reconstruction efficiencies and background studies six streams of generic Monte Carlo (MC) samples of all 4 types (charged, mixed, charm and uds) are used. For the  $\Sigma^+\pi^0\pi^0$  mode  $6 \times 2.138 \times 10^6$  events of signal MC are prepared, utilizing the *mcproduzeh* package to generate experiment dependent data. This number is consistent with a relative  $\mathcal{B}(\Sigma^+\pi^0\pi^0)/\mathcal{B}(\Sigma^+\pi^+\pi^-)$  of 0.5 exclusively from  $c\bar{c}$  events. The decay model used is PHOTOS PHSP. Both analysis and MC production is performed with the library version BELLE\_LEVEL b20090127\_0910.

Hyperons are reconstructed using the following channels:

$$\Lambda^0 \rightarrow p\pi^- \quad (63.9 \pm 0.5\%) \quad (3.1)$$

$$\Sigma^+ \rightarrow p\pi^0 \quad (51.57 \pm 0.3\%) \quad (3.2)$$

$$\Sigma^0 \rightarrow \Lambda\gamma \quad (100\%) \quad (3.3)$$

## 3.2 Preselection

### Charged final state particles

- A general Particle Identification (PID) likelihood cut of  $\text{PID} > 0.6$  is applied. After a first optimization a scan over possible PID cut combinations is performed. Only in the reference channel a stricter requirement is found to be beneficial. The values chosen are  $\mathcal{L}(p\pi) > 0.9$  and  $\mathcal{L}(pK) > 0.9$ , symmetrical to confirm with the proton cut efficiency study.
- Protons used in the reconstruction of the  $\Sigma^+$  baryon are discarded if the radial component of their impact parameter is smaller than 0.03 cm.
- Radial and beam direction impact parameters for charged tracks directly from  $\Lambda_c$  are cut at 2 and 4 cm.

### Uncharged final state particles

- Photons are required to be associated with a calorimeter energy larger than 40 MeV.
- $\pi^0$  with momentum in the laboratory frame exceeding 100 MeV are taken from `mdst_pi0`.

### Hyperons

$\Lambda^0$  is reconstructed from the `mdst_Vee2`. The mass window for  $M(p\pi)$  lies between 1.113 and 1.118  $\text{GeV}/c^2$ . No further cuts are applied at this stage.

$\Sigma^0$  is formed by combining  $\Lambda^0\gamma$  in an invariant mass region between 1.1876 and 1.1976  $\text{GeV}/c^2$ . As with  $\Lambda^0$  no further cuts are applied.

|             |                                       |
|-------------|---------------------------------------|
| $\Sigma^+$  | $1.187 < M < 1.955 \text{ GeV}/c^2$   |
| $\Sigma^0$  | $1.1876 < M < 1.1976 \text{ GeV}/c^2$ |
| $\Lambda^0$ | $1.113 < M < 1.118 \text{ GeV}/c^2$   |
| $\pi^0$     | $134.9766 \pm 15 \text{ MeV}/c^2$     |

Table 3.1: Invariant mass windows

$\Sigma^+$  reconstruction follows an approach suggested by John M. Yelton [38]. It utilizes that charged tracks from long lived Hyperons often are associated with a significant impact parameter. The momenta of a charged track that suffices  $dr > 0.3$  and a  $\pi^0$  candidate are added. This vector, the interaction point (IP) and the impact parameters of the proton are used to calculate a first trial vertex. Should the measured flight distance be negative the candidate is discarded. Using this trial vertex the mass constraint fit for the pion is redone, leading to improved resolution. Now a kinetic vertex fit can be performed, discarding all candidates with  $\chi^2$  bigger than 100. In the next step mass cuts on  $M(p\pi^0)$  and  $M(\gamma\gamma)$  are applied. The limits are 1.187 and 1.1955  $\text{GeV}/c^2$  for the former and  $134.97 \pm 15 \text{ MeV}/c^2$  for the latter. Finally the mass constraint is also done for the  $\Sigma^+$  candidate.

$\Lambda_c^+$  To reduce combinatorial and  $B-\bar{B}$  background the scaled momentum, defined as  $x = p/p_{max}$ , where  $p$  stands for the candidate momentum and  $p_{max}$  for the maximal possible momentum, is required to exceed 0.5. In modes with several charged tracks a vertex fit is performed and only successful fits with a  $\chi^2$  under 100 are kept.

### 3.3 BDT and Input variables

Boosted Decision Trees (BDT) are a Multivariate Data Analysis technique that improves on Binary Decision Trees. The latter are developed by searching for the best discriminating variable and applying a cut determined by maximising a figure of merit. This splits the data set into two sub-sets, one defined as signal, the other as background. The process is repeated for each sub-set until a threshold number of entries is reached. An event is then classified by the final sub-set it ends up part of. Applying this process to a known sample is called training. The risk in using this method is that a very deep tree might perfectly classify the sample used for training while being next to useless on an independent data set. This risk is minimized by BDTs by only training very shallow decision trees, usually only three to four nodes deep. Then wrongly classified events are reweighed and used for a new tree. After

several hundred repetitions the average of the individual trees determines the final classification for each event.

Events that survive the preselection are used in the training of BDTs with the ROOT TMVA package version 4.2.0 using the following input parameters.

- The scaled momentum of the candidate and hyperons.
- All charged final state particle and  $\pi^0$  candidate momenta in the center of beam mass frame (cbm) frame.
- The cluster energy and angle of detected  $\gamma$  in the EMC.
- The cosine of the angle between the two  $\gamma$  from  $\pi^0$  in laboratory frame. This parameter is effective to reduce combinatorial background.
- The  $\chi^2$  of the final vertex fit in modes with several charged daughter products.
- A binary flag obtained by forming  $\pi^0$  candidates from all possible two photon combinations starting from the most energetic photons. Combinations with invariant mass in the range of  $\pm 15$  MeV are selected as candidates and the photons used are excluded when searching for further candidates[37].
- The output of the Lambda finder.
- Impact parameters in radial and beam direction (dr, dz) for all charged tracks.

One stream of Monte Carlo data is used for training in all decay modes and tested on the remaining five except the  $\Sigma^+\pi^0\pi^0$  channel where training is performed twice using halve the data for each. For the purpose of BDT training only correctly reconstructed candidates are used as the signal sample while all other contributions are treated as background events. Separate treatment of partially reconstructed candidates using a wrong  $\gamma$  does not lead to improvement in terms of FoM. In case of multiple candidates in one event the highest ranking one in the BDT classifier is selected. The number of surviving events after each step is summarized in table 3.2.

$\Sigma^+\pi^+\pi^-$  candidates are considered for training and Figure of Merit (FoM) optimization if they fall in an invariant mass window between 2.266 GeV and 2.306 GeV. The distribution for both signal and background in the input variables is plotted in the figures 3.1 and 3.2, split only for reasons of space.

|                      | True Events     |            |              |         |                |
|----------------------|-----------------|------------|--------------|---------|----------------|
|                      | HadronB $Y(4S)$ | $c\bar{c}$ | preselection | BDT     | best candidate |
| $pK^-\pi^+$          | 10,646,869      | 6,561,862  | 481,516      | 360,508 | 330,686        |
| $\Sigma^+\pi^+\pi^-$ | 6,933,758       | 4,275,127  | 121,366      | 103,245 | 85,533         |
| $\Sigma^+\pi^0\pi^0$ | -               | 2,137,696  | 24384        | 10617   | 8268           |
| $\Sigma^0\pi^+\pi^0$ | 3,467,638       | 2,136,099  | 54,026       | 28533   | 24,067         |

Table 3.2: True events in one stream MC + CC

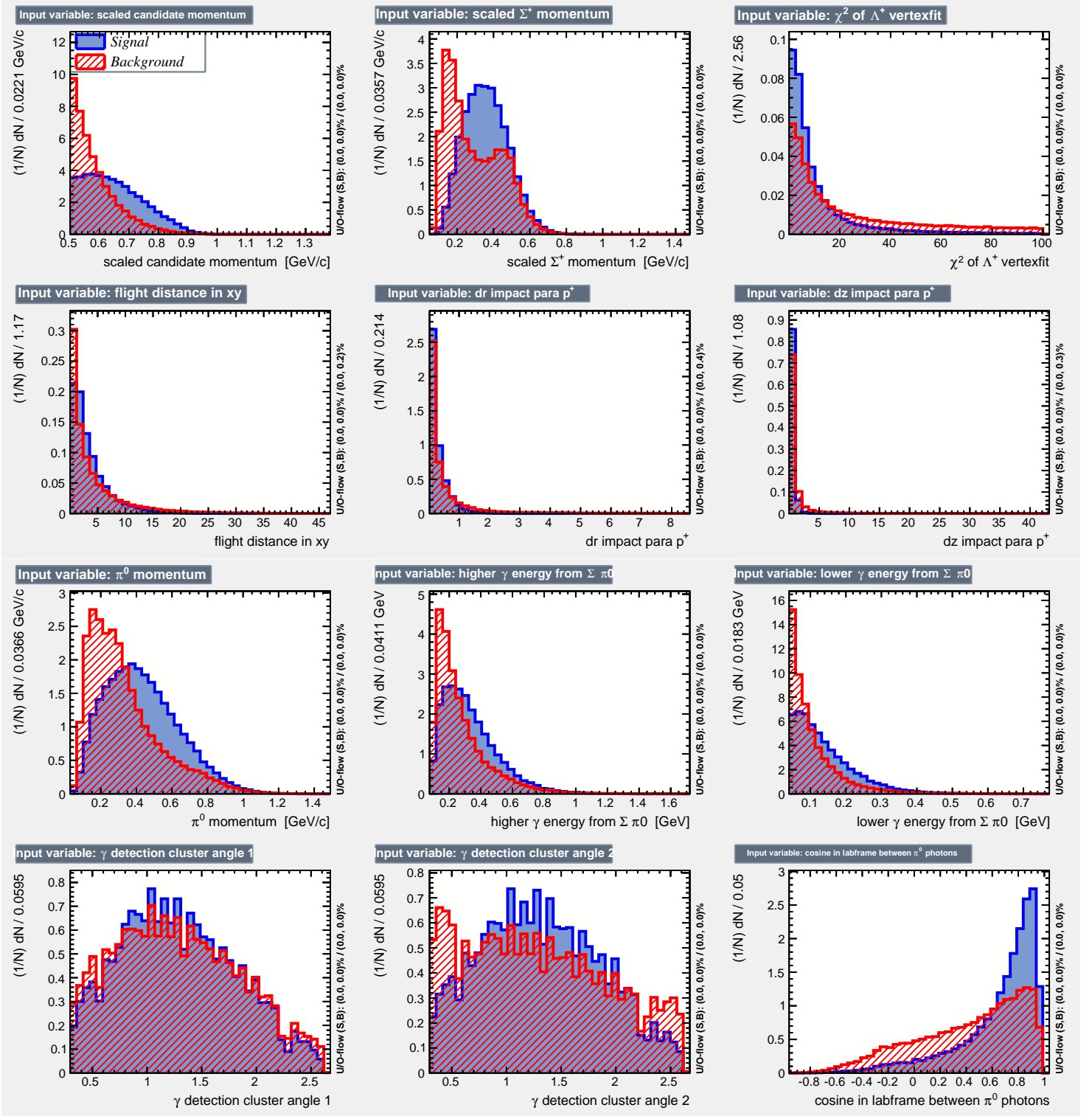


Figure 3.1: Input variables for BDT training on  $\Sigma^+\pi^+\pi^-$  candidates. From top left to bottom right: Scaled momentum for  $\Lambda_c$  and  $\Sigma^+$  candidates,  $\chi^2$  of the  $\Lambda_c$  vertexfit, flight distance of  $\Sigma^+$  in xy - plane, proton impact parameters,  $\pi^0$  momentum, higher and lower photon energy and their respective ECL detection angle and the cosine between the  $\pi^0$  photons in the laboratory frame. continued in 3.2

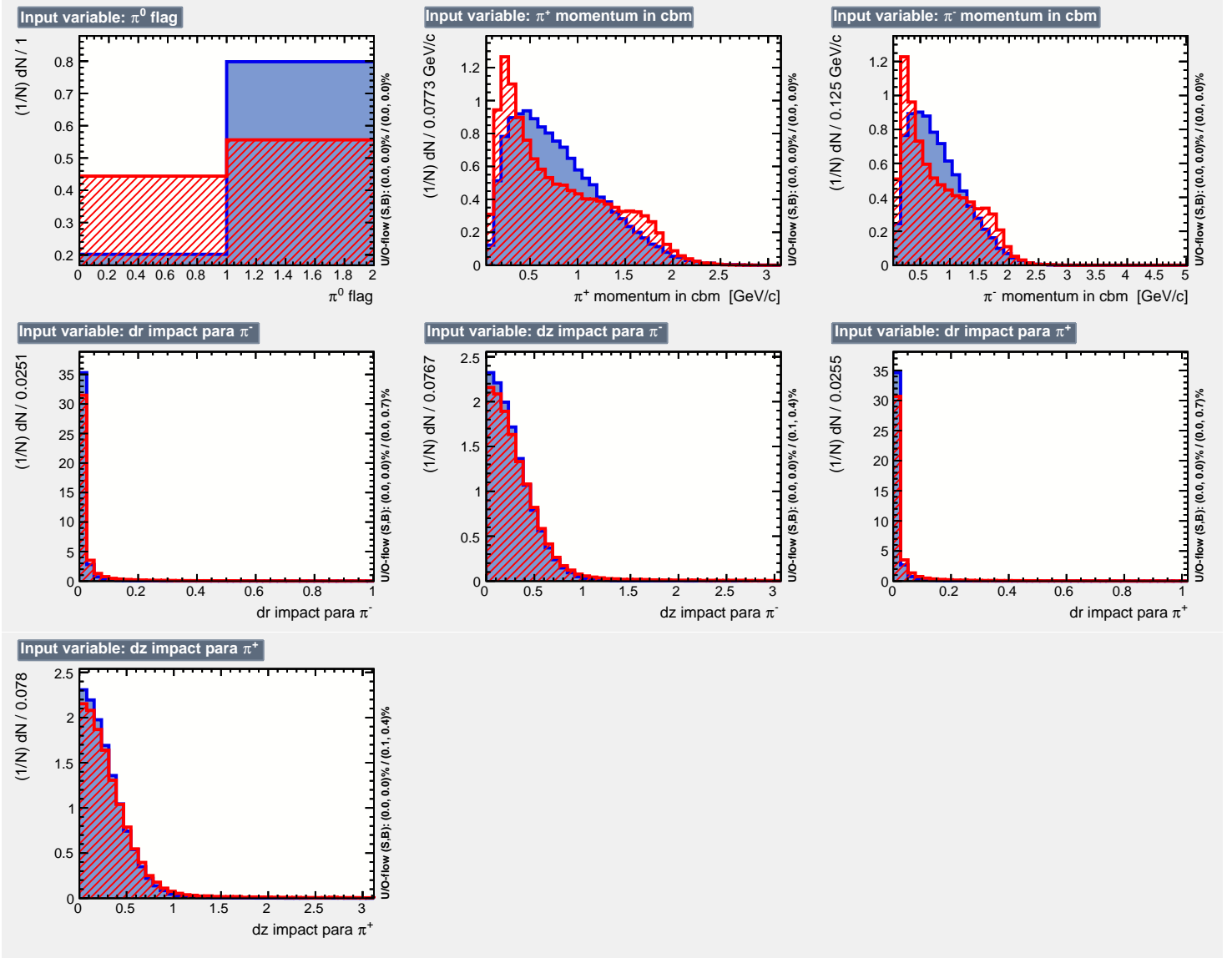


Figure 3.2: Continued from Fig. 3.1. Input variables for BDT training on  $\Sigma^+\pi^+\pi^-$  candidates. From top left to bottom right:  $\pi^0$  flag, charged pion momenta in cbm frame and impact parameter for pions.

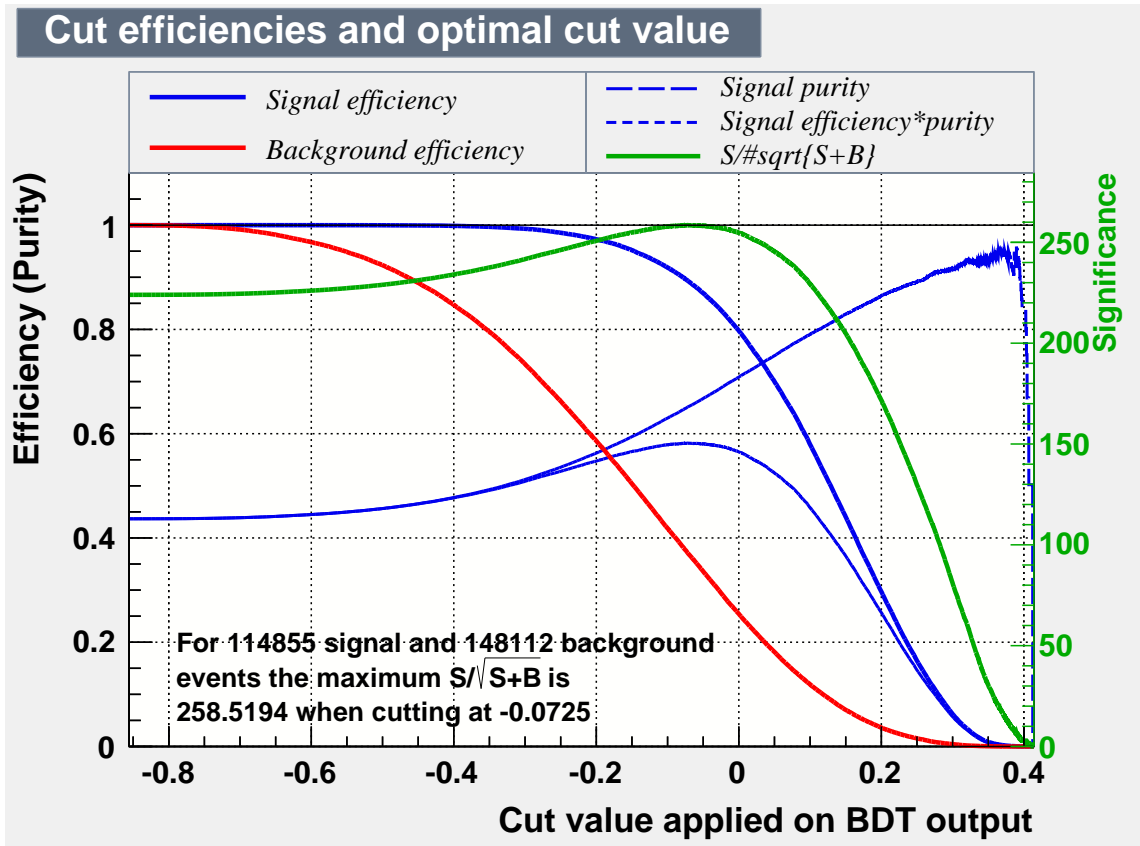


Figure 3.3: Cut efficiency for  $\Sigma^+\pi^+\pi^-$  candidates on test sample. Testing the optimized selection criteria on another stream results in a FoM of 254.953

$\Sigma^+\pi^0\pi^0$  The signal region for  $\Lambda_c$  candidates reconstructed in the  $\Sigma^+\pi^0\pi^0$  channel is broadened to 2.22 GeV and 2.306 GeV to account for the tail toward low energies caused by the  $\gamma$  resolution. The distribution for both signal and background in the input variables is described in Fig. 3.4 and 3.5.

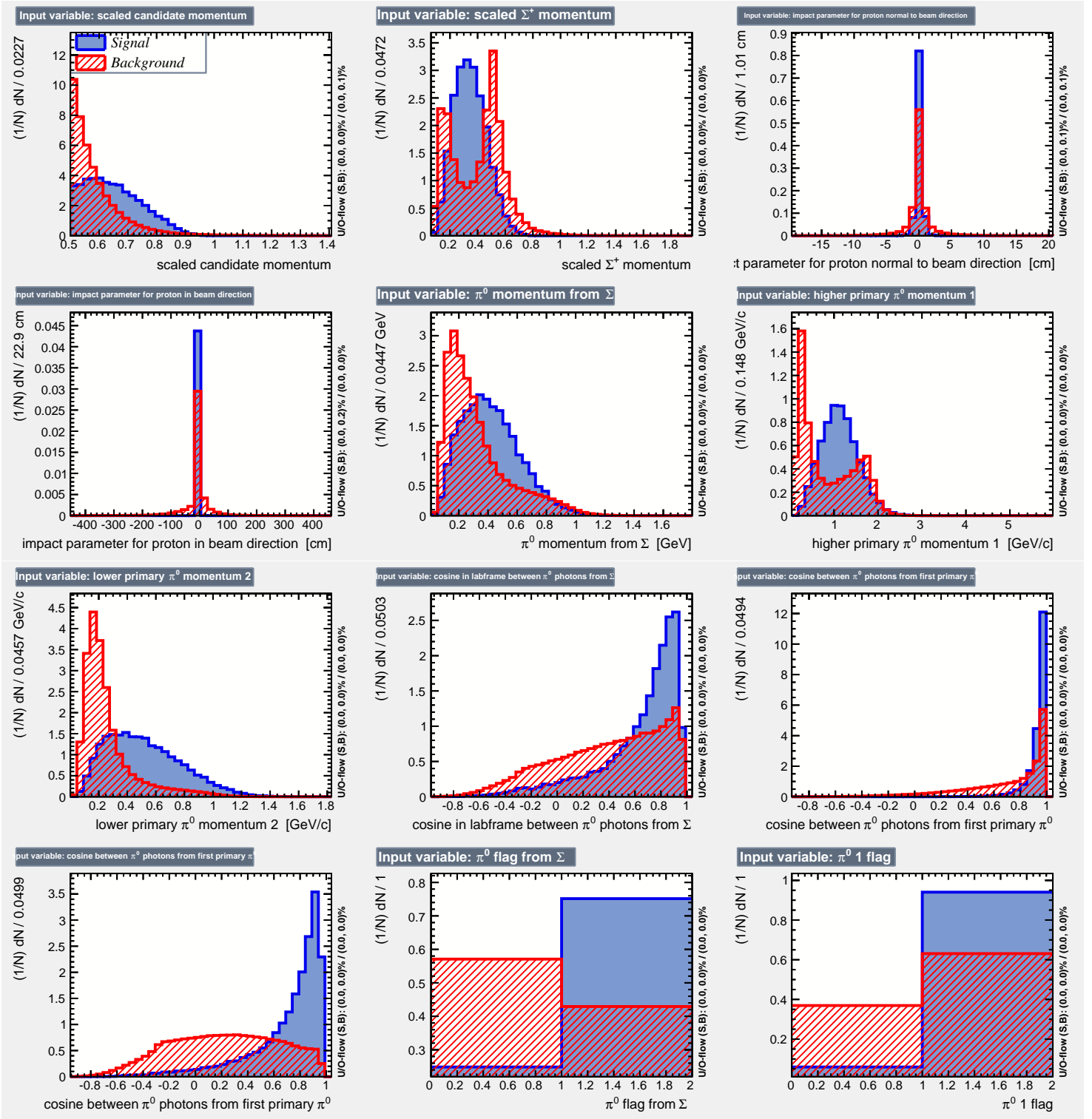


Figure 3.4: Input variables for BDT training on  $\Sigma^+\pi^0\pi^0$  candidates. From top left to bottom right: Scaled momentum for  $\Lambda_c$ ,  $\Sigma^+$ , proton impact parameters and cbm momentum for the secondary  $\pi^0$ , faster and slower primary  $\pi^0$  and their corresponding photon cosines in laboratory frame and the  $\pi^0$  flag for the  $\Sigma$  and faster primary  $\pi^0$ . Continued in Fig. 3.5

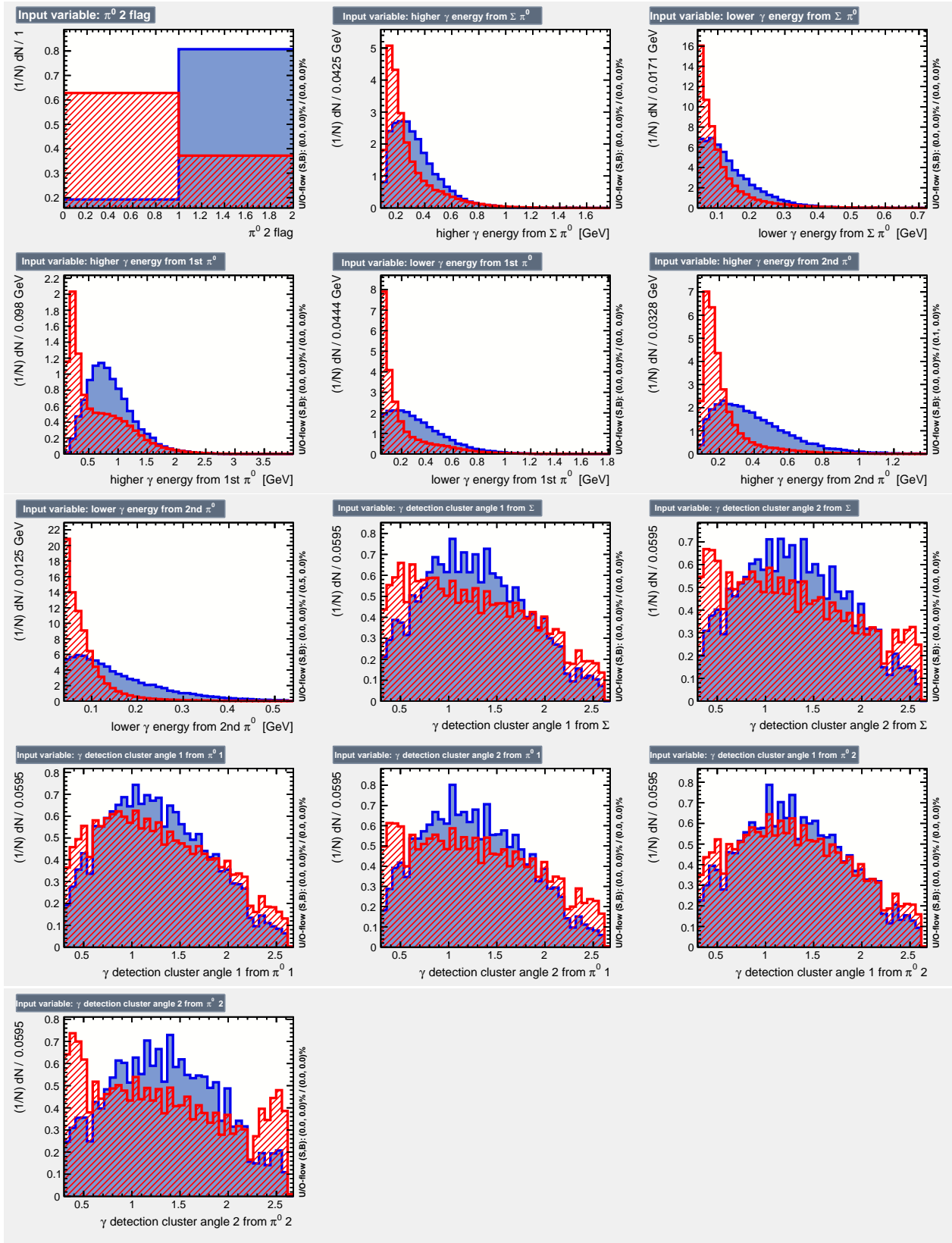


Figure 3.5: Continued from Fig. 3.4. Input variables for BDT training on  $\Sigma^+\pi^0\pi^0$  candidates. From top left to bottom right:  $\pi^0$  flag for the slower primary  $\pi^0$ , energy of  $\pi^0$  photons in order of  $\Sigma^+$  faster and slower.

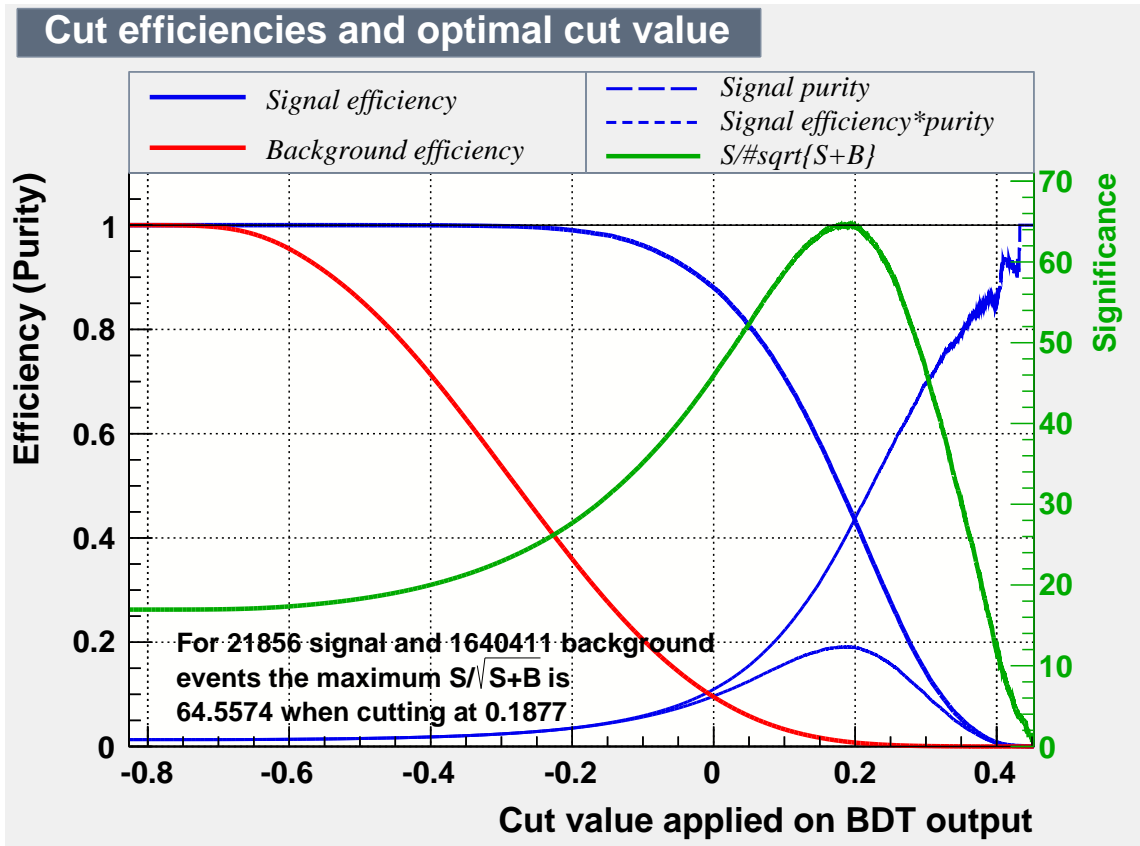


Figure 3.6: Cut efficiency for  $\Sigma^+\pi^0\pi^0$  candidates on test sample. A different MC stream leads to FoM 60.2526 at BDT > 0.175.

$\Sigma^0\pi^+\pi^0$  candidates use the same signal region of 2.22 GeV and 2.306 GeV as the previous mode. The distribution of the input parameters for signal and background are plotted in figures 3.7 and 3.8

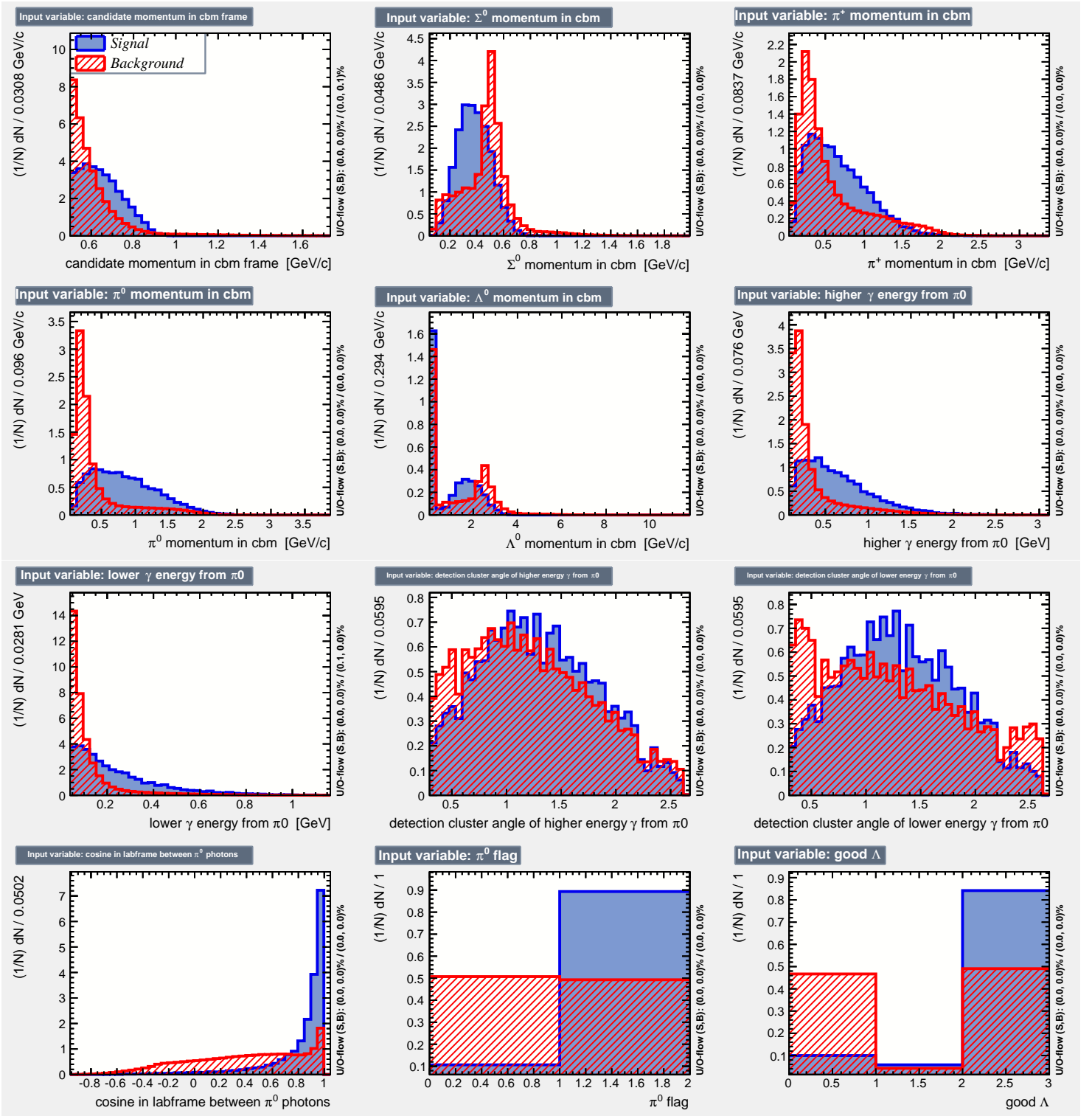


Figure 3.7: Input variables for BDT training on  $\Sigma^0\pi^+\pi^0$  candidates. From top left to bottom right: Scaled momentum for  $\Lambda_c$  and  $\Sigma^0$ , cbm momentum for  $\pi^+$ ,  $\pi^0$  and  $\Lambda^0$  candidate, higher and lower  $\pi^0$  photon energies, their corresponding ECL detection clusters and the cosine between their trajectories in laboratory frame, the  $\pi^0$  flag, the good  $\Lambda$  finder output and the  $\Sigma^0$  photon energy and ECL angle. Continued in Fig. 3.8

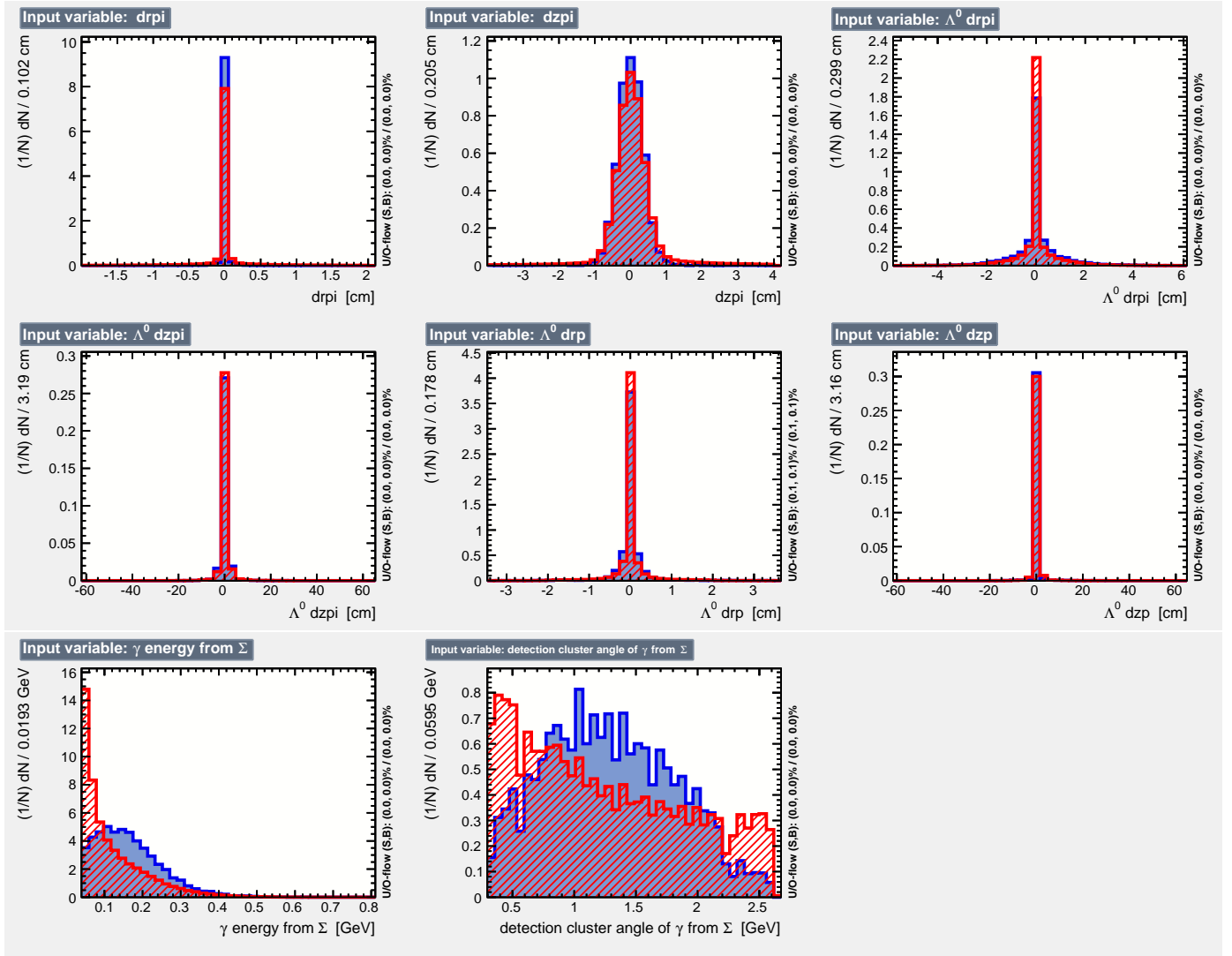


Figure 3.8: Continued from Fig. 3.7. Input variables for BDT training on  $\Sigma^0\pi^+\pi^0$  candidates. From top left to bottom right:  $\Lambda_c$ ,  $\Sigma^0$ ,  $\pi^+$ ,  $\pi^0$  and  $\Lambda^0$  candidate momentum in cbm frame, higher and lower  $\pi^0$  photon energies, their corresponding ECL detection clusters and the cosine between their trajectories in laboratory frame, the  $\pi^0$  flag, the good  $\Lambda$  finder output and the  $\Sigma^0$  photon energy and ECL angle.

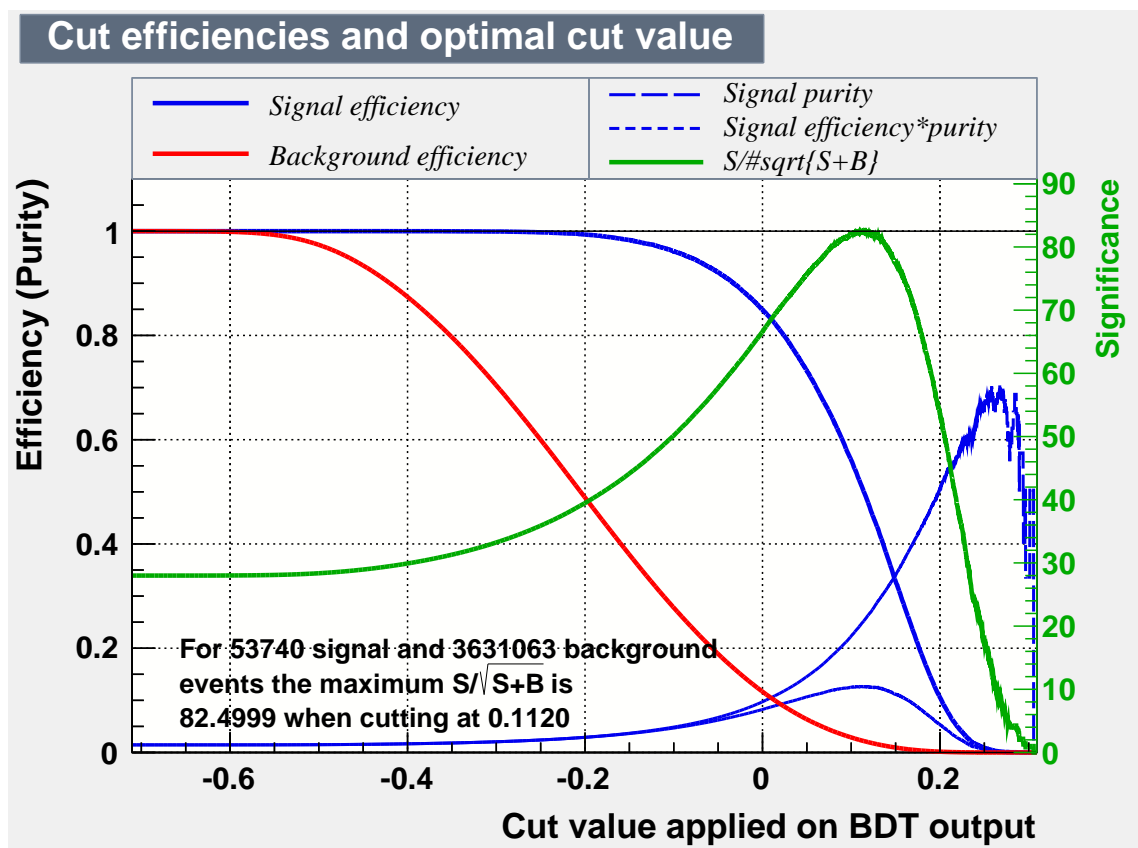


Figure 3.9: Cut efficiency for  $\Sigma^0\pi^+\pi^0$  candidates on independent test sample: 81.4.

$pK^-\pi^+$  The signal region used is between 2.266 GeV and 2.306 GeV, the input parameters are plotted in Fig. 3.10.

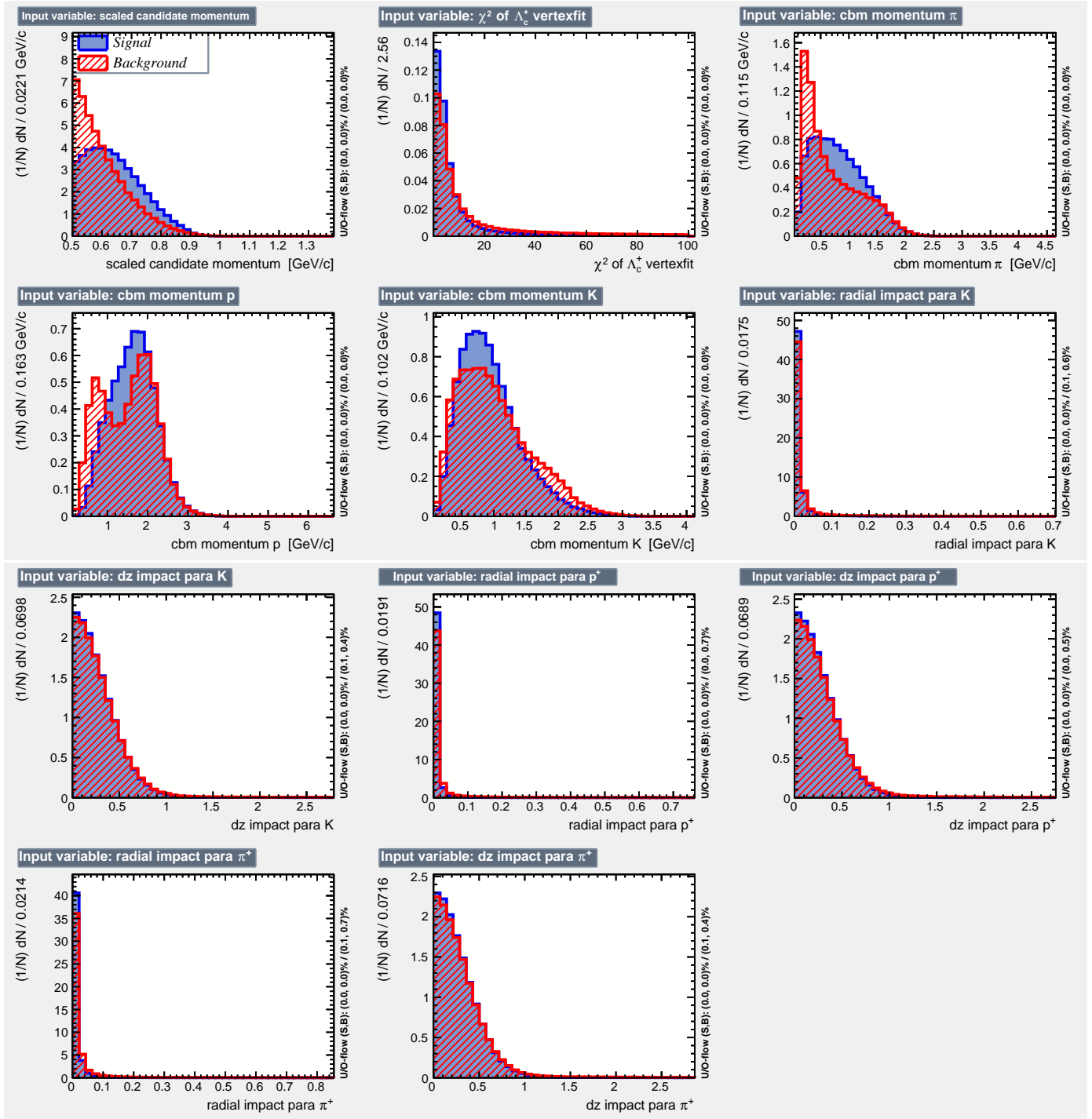


Figure 3.10: Input variables for BDT training on  $pK^- \pi^+$  candidates. From top left to bottom right: Scaled momentum of  $\Lambda_c$  candidates, cbm momentum of pion proton and kaon and impact parameters for  $K^-$ ,  $p$ ,  $\pi^-$ .

### 3.4 Background

$\Sigma^+\pi^+\pi^-$  Several non random background components can be identified.

- A  $\Lambda_c$  candidate reconstructed using one incorrect  $\gamma$  leads to a broad peak around the nominal mass, of 6.6% signal yield in the fitting region.
- Decay channels with more final state particles like  $\Lambda_c \rightarrow \Sigma^+\eta$  lead to a small enhancement below 2.2 GeV/ $c^2$ .
- $\Lambda_c \rightarrow \Sigma^+\omega$  generates a small peak at nominal mass for the case of  $\omega \rightarrow \pi\pi$  and otherwise a broad enhancement below 2.2 GeV/ $c^2$ .

By limiting the background fitting range to an interval of 2.2 to 2.4 GeV/ $c^2$  most of contributions can be ignored. Since the  $\Sigma^+\omega$  component is unlikely to contribute to the  $\Sigma\pi$  charge exchange and  $\mathcal{B}(\omega \rightarrow \pi\pi)$  it would be considered background for the determination of the scattering length and can be eliminated by a veto on the invariant mass of the two pion combination around the nominal  $\omega$  mass of  $\pm 30$  MeV, at the cost of reducing yield by 10%. For the  $\mathcal{B}(\Sigma^+\pi^+\pi^-)$  it is included as signal.

$\Sigma^0\pi^+\pi^0$  Several background components can be identified:

- A  $\Lambda_c$  candidate reconstructed using one incorrect  $\gamma$  leads to a broad peak around the nominal mass, of 21% signal yield.
- $\Lambda_c \rightarrow \Lambda\pi^+\pi^0$  ( $3.6 \pm 1.3\%$ ) leads to a peak at 2.38 GeV, close to the signal.
- $\Lambda_c \rightarrow \Lambda\rho^+$  ( $3.6 \pm 1.3\%$ )
- $\Lambda_c \rightarrow \Sigma^0\pi^+$  ( $1.05 \pm 0.28\%$ ) (over 2.4 GeV/ $c^2$ )
- $\Xi_c^+ \rightarrow \Xi^0\rho^+$

Several components including  $\rho^+$  can be strongly reduced by using a veto on the invariant  $\pi\pi$  mass between 0.65 and 0.95 GeV at the cost of 37% of signal yield. The effect on the background can be seen in Fig. 3.12. The  $\Lambda\pi\pi$  and signal correlated component are fitted separately. The remaining  $\Lambda_c \rightarrow \Lambda\rho^+$  is included in the background polynomial.

### Background components for $\Sigma^+\pi^+\pi^-$

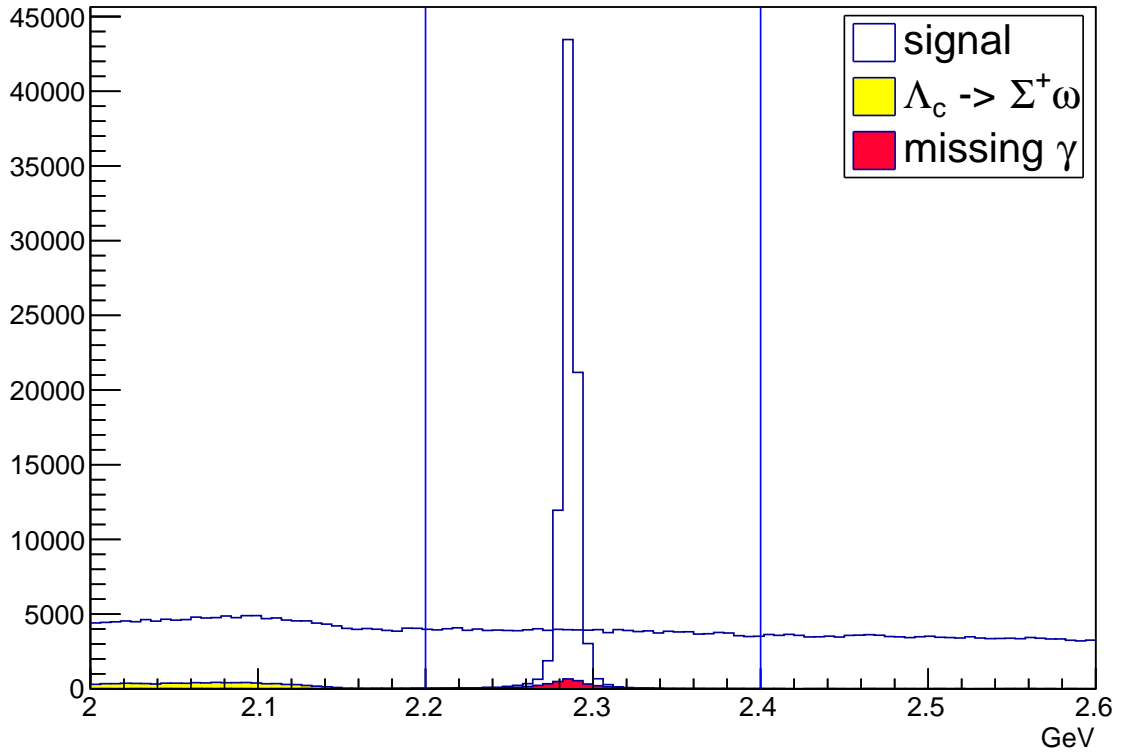
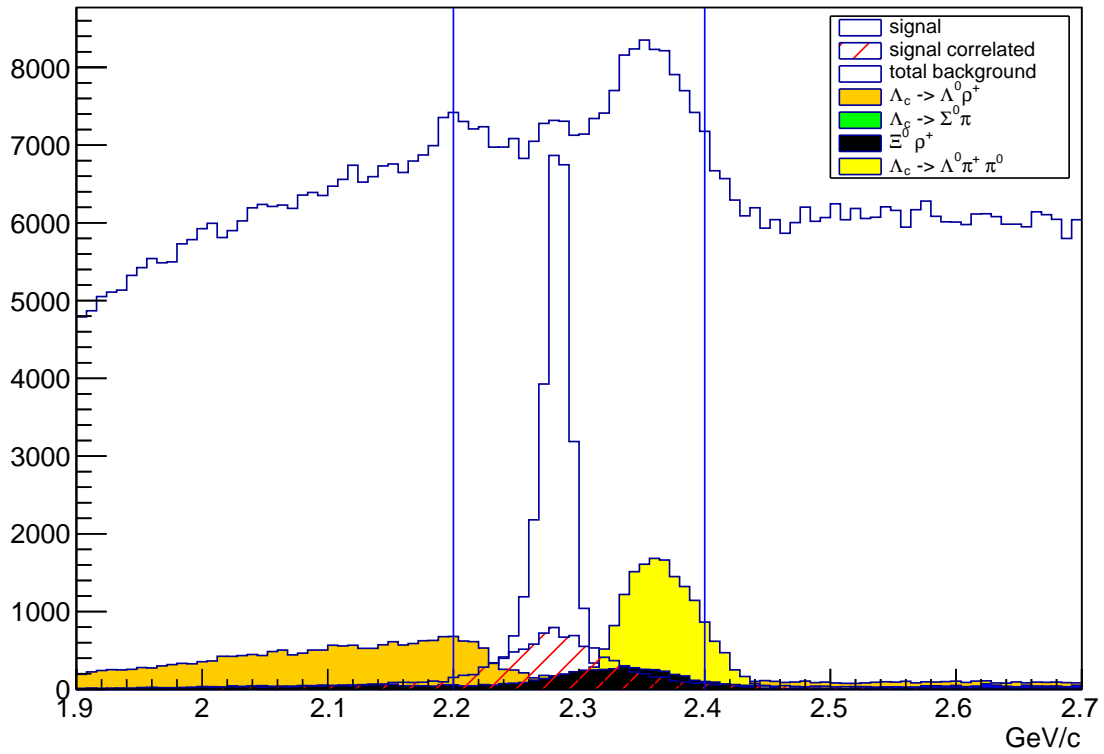


Figure 3.11: Background components and fitting range for  $\Sigma^+\pi^+\pi^-$  channel. The contribution of candidates reconstructed using a wrong  $\gamma$  amounts to 6.5% of signal strength over the whole fitting range.

### Background components



### Background components

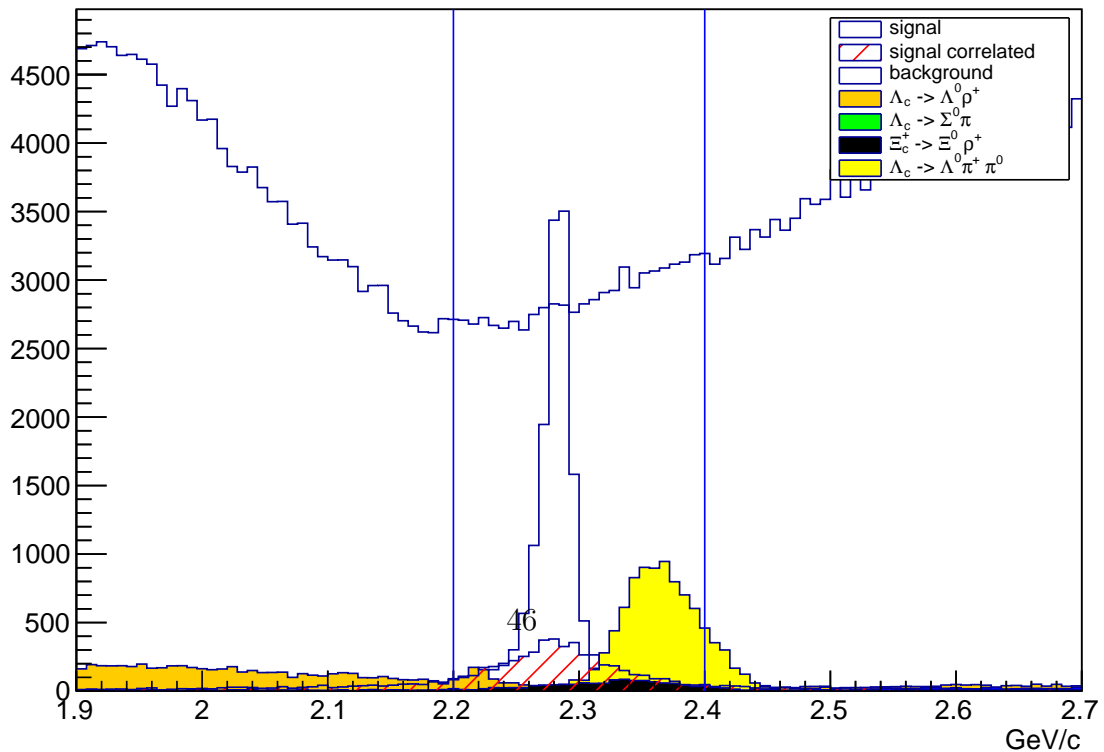


Figure 3.12: Background components in  $\Sigma^0 \pi^+ \pi^0$  channel. Top Fig. without, bottom with cut on the  $\rho^+$  invariant mass.

## Background components for $\Sigma^+\pi^0\pi^0$

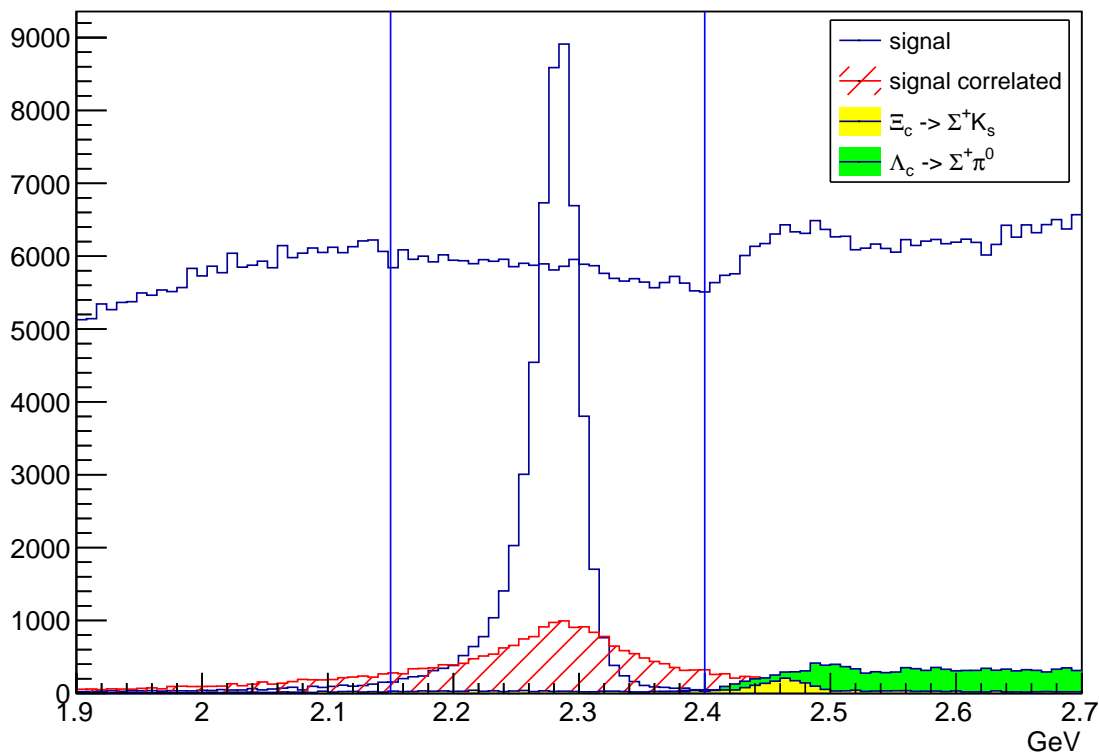


Figure 3.13: Background components in  $\Sigma^+\pi^0\pi^0$  channel in the fitting range from 2.1 GeV to 2.43 GeV

### $\Sigma^+\pi^0\pi^0$

- $\Lambda_c$  candidates reconstructed using one incorrect  $\gamma$  lead to a broad peak around the nominal mass, of 22% signal yield.
- $\Lambda_c \rightarrow pK_s\pi^0$  contributes to a slight enhancement around the nominal  $\Lambda_c$  mass.
- $\Xi_c \rightarrow \Sigma^+K_s$  leads to an enhancement between 2.43 and 2.49 GeV/c.

The third contribution is dealt with by limiting the fitting range, the other two components are fitted separately.

$pK^-\pi^+$  No specific background components are accounted for.

### Background components for $pK\pi$

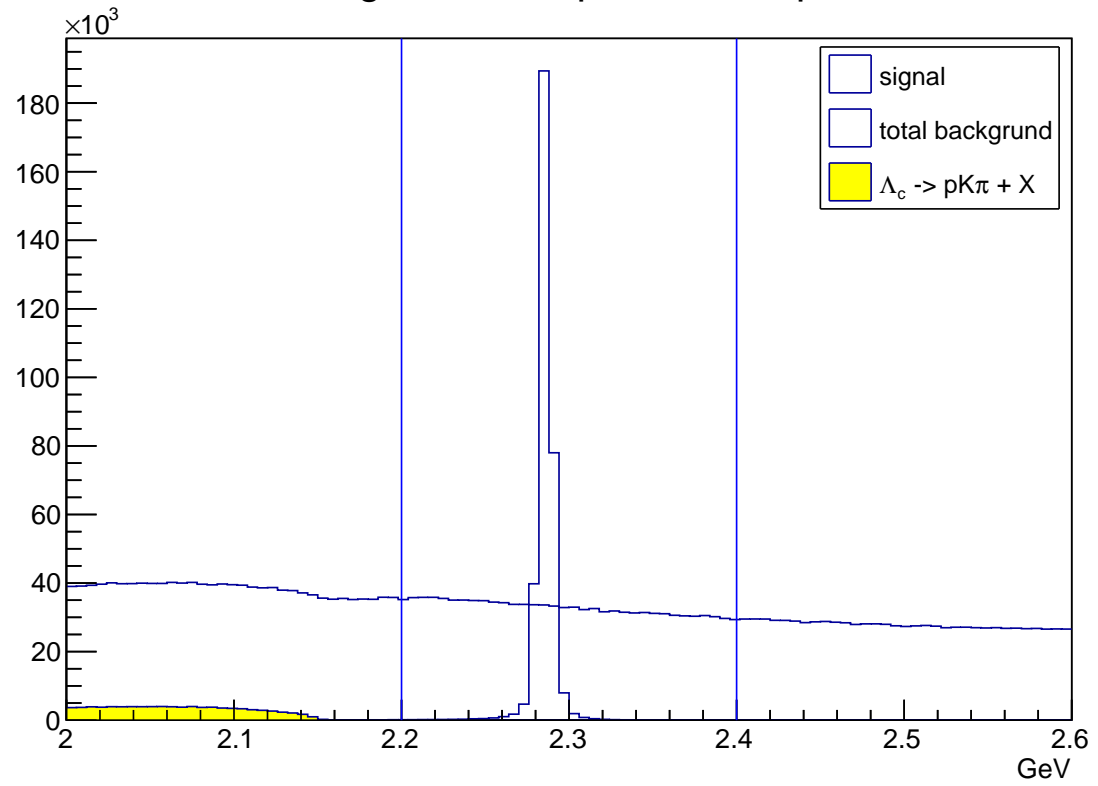


Figure 3.14: Background components in the  $pK^-\pi^+$  channel. Fitting range from 2.2 GeV to 2.4 GeV

### 3.5 Yield extraction

The fitting process follows several steps: First four streams of generic Monte Carlo of all kinds (charged, charm, uds, and mixed) are used to determine the probability density function (PDF) shapes and parameters on each component separately. Then one stream is used as pseudo real data to determine the resulting yield. Finally the procedure is repeated five times, using different combinations of MC streams in order to test for fit biases. The PDFs used are listed in table 3.3. The Crystal Ball function, named after the Crystal Ball Collaboration is a PDF used to model lossy processes in high energy physics. It consists of a Gaussian core and a power-law tail below a certain threshold.

Table 3.3: Table of PDFs

|                      | Signal                      | Background                | Correlated                           | $\Lambda^0\pi^+\pi^0$ |
|----------------------|-----------------------------|---------------------------|--------------------------------------|-----------------------|
| $pK^-\pi^+$          | 2 Gaussians + Breit-Wigner  | Chebychev polynom order 3 | -                                    | -                     |
| range (GeV/c)        | 2.26 - 2.31                 | 2.2 - 2.4                 | -                                    | -                     |
| $\chi^2/n.d.f.$      | 5                           | 1 - 1.8                   | -                                    | -                     |
| $\Sigma^+\pi^+\pi^-$ | Gauss + Breit-Wigner        | Chebychev polynom order 2 | -                                    | -                     |
| range (GeV/c)        | 2.26 - 2.31                 | 2.2 - 2.4                 | -                                    | -                     |
| $\chi^2/n.d.f.$      | 4.5 -5                      | 1.2                       | -                                    | -                     |
| $\Sigma^0\pi^+\pi^0$ | Breit-Wigner + Crystal Ball | Chebychev polynom order 1 | Breit-Wigner + Bifurcating Gaussian  | Gauss + Crystal Ball  |
| range (GeV/c)        | 2.18 - 2.36                 | 2.2 - 2.4                 | 2.1 - 2.5                            | 2.25 - 2.45           |
| $\chi^2/n.d.f.$      | 1.25 - 1.8                  | 1.4 -1.5                  | 2.5 - 2.7                            | 1.3 -1.56             |
| $\Sigma^+\pi^0\pi^0$ | Gauss + Crystal Ball        | Chebychev polynom order 1 | Breit -Wigner + Bifurcating Gaussian | -                     |
| range (GeV/c)        | 2.1 - 2.4                   | 2.16 - 2.4                | 2 - 2.6                              | -                     |
| $\chi^2/n.d.f.$      | 1.4 - 1.6                   | 1.1 - 1.5                 | 0.8 -1                               | -                     |

$\Sigma^+\pi^+\pi^-$  The signal correlated component of  $M[\Sigma\pi\pi]$  is fitted together with the signal component. The ratio in the fitting region of 2.2 to 2.4 GeV is fixed to 6.65% from Monte Carlo. The signal PDF is modelled as a Gaussian and a Bifurcating Gaussian, the background as a Chebychev Polynomial of the second order. Parameters for the signal component are determined in a range of 2.26 to

2.31 GeV. The fits for the separate components can be seen in Fig. 3.15, the combined fits and yields compared with MC truth in Fig. 3.16. The fitted parameters are listed in table 5.1 and 5.2.

$\Sigma^0\pi^+\pi^0$  Signal, the signal correlated component and  $\Lambda_c \rightarrow \Lambda\pi\pi$  are fitted separately. The signal is described as a Breit - Wigner and Crystal Ball function, determined between 2.18 and 2.36 GeV, the correlated component as a Breit - Wigner and Bifurcating Gaussian on 2.15 to 2.5 GeV. The parameters are listed in table 5.3 and 5.4, the separate PDF components in 3.20 and the total PDF as well as the yield compared to MC truth in Fig. 3.21

$\Sigma^+\pi^0\pi^0$  The signal component is parametrized with a Gaussian and a Crystal Ball function, the signal correlated component with a nonrelativistic Breit-Wigner function and a bifurcated Gaussian. The background is modelled as a Chebychev Polynomial of the second order. The ranges are 2.1 to 2.4 GeV, 2 to 2.6 GeV and 2.16 to 2.4 GeV respectively. Figure 3.20 shows the fits for the separate components, Fig. 3.21 the complete fits and the difference between yields and MCtruth. The fit parameters and yields are listed in table 5.5 and 5.6. .

$p\mathbf{K}^-\pi^+$  The signal component is modelled as two Gaussians and a Breit-Wigner function, the background as a Chebychev Polynomial of the third order. The ranges are 2.26 to 2.31 GeV and 2.2 to 2.4 GeV. The fit parameters and yields are listed in table 5.7 and 5.8, Figure 3.22 shows the fits for the separate components, Fig. 3.23 the final fit and the yield.

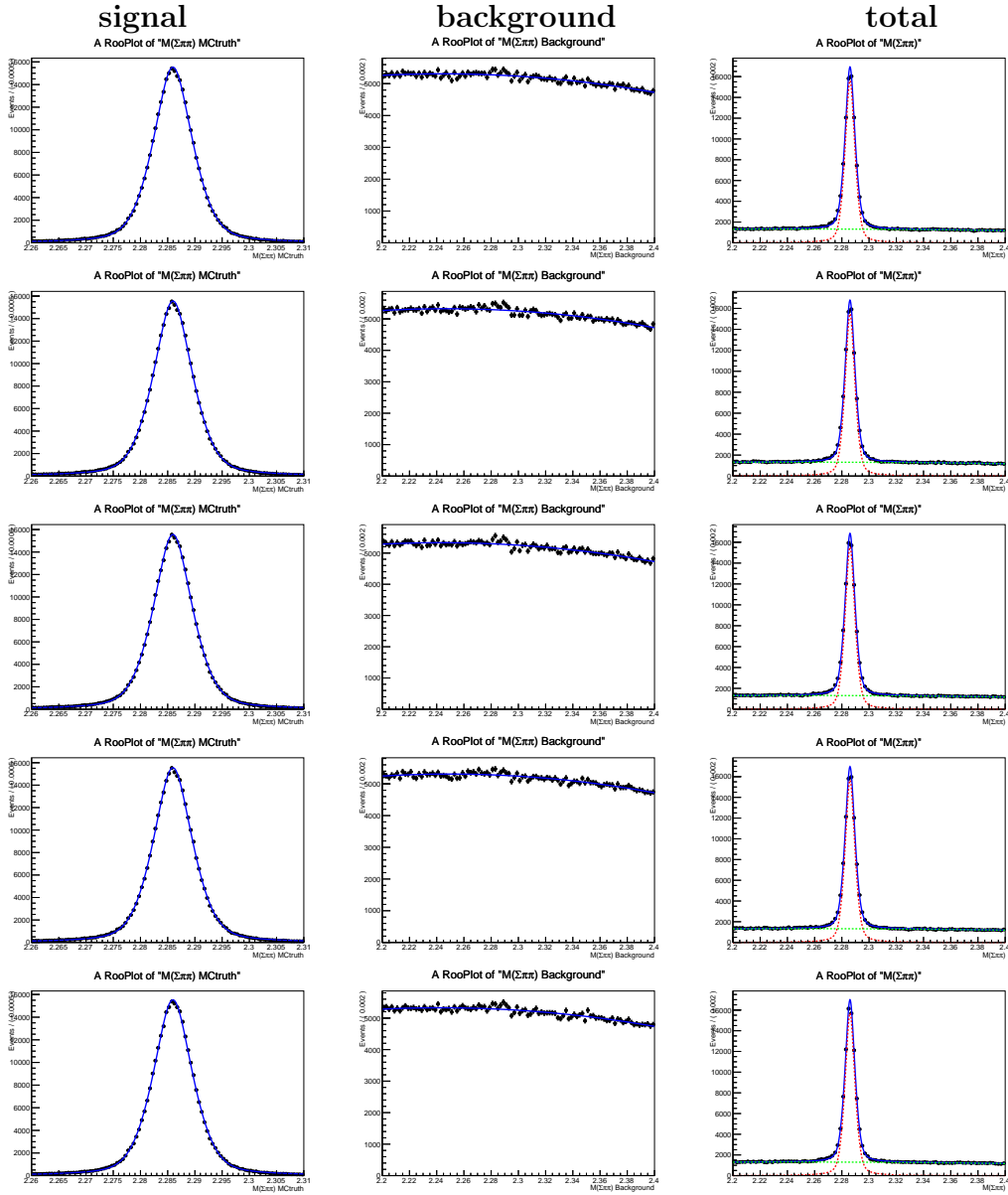


Figure 3.15: 5  $\Sigma^+\pi^+\pi^-$  PDFs. From top left to lower right: Signal, parametrized as a Gaussian and a Breit - Wigner function, background parametrized as a Chebychev Polynomial of the order two and total PDFs with signal (red) and background (green) for MC stream 1 - 5. To determine parameters four of five MC streams are used. The total PDF is plotted for the remaining stream.

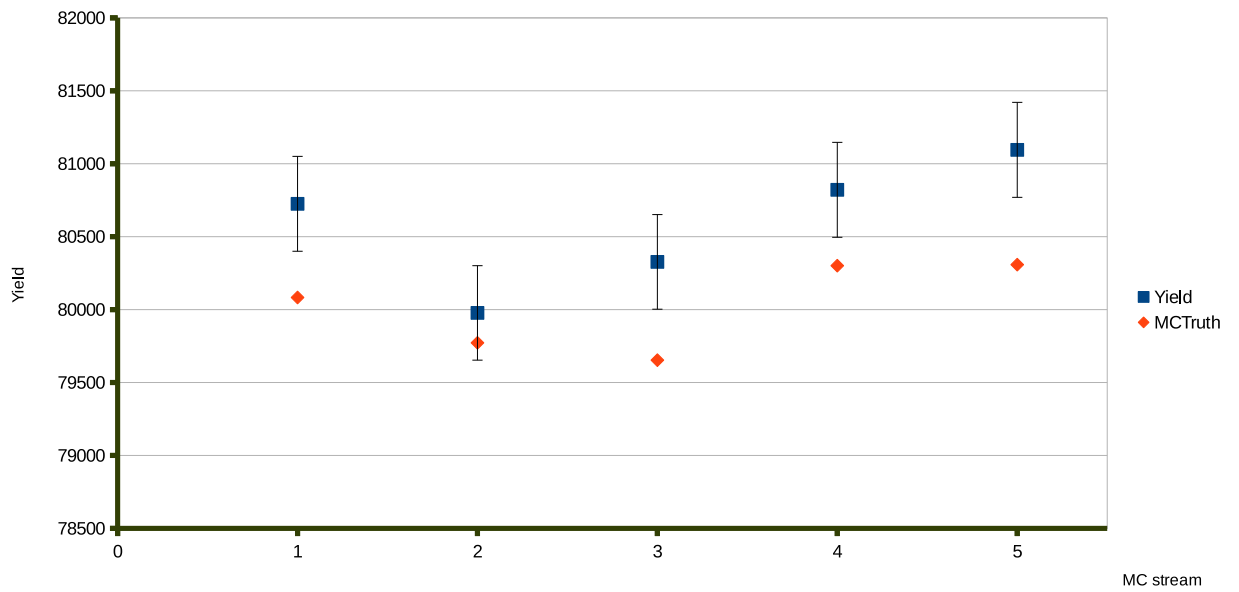


Figure 3.16: Yield for signal and correlated component with statistical error compared to MC truth for the  $\Sigma^+\pi^+\pi^-$  channel.

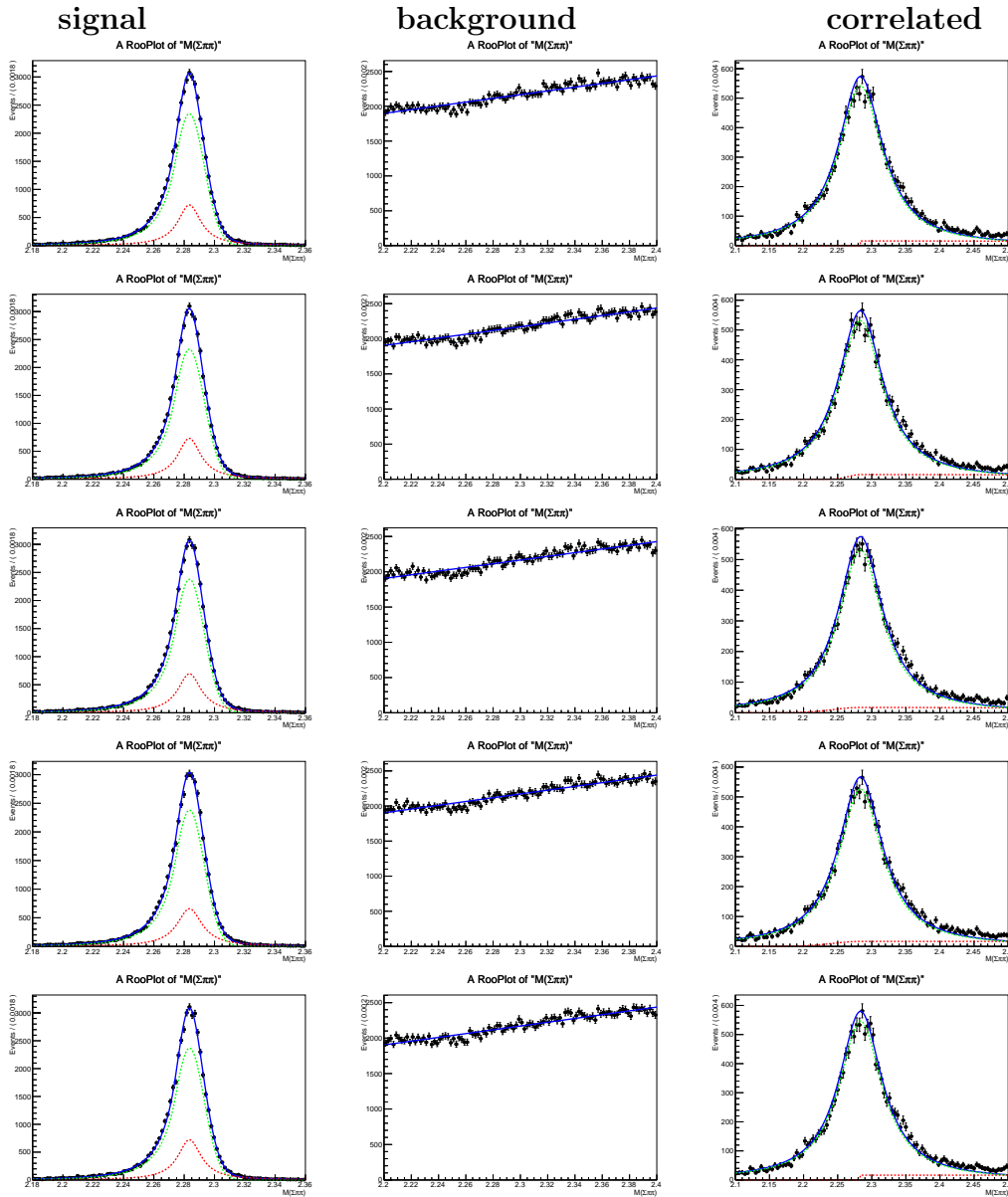


Figure 3.17:  $\Sigma^0\pi^+\pi^0$  PDFs. From top left to bottom right: Signal, parametrized as a Crystal Ball (green) and a nonrelativistic Breit-Wigner function (red), background parametrized as a Chebychev Polynomial of the first order and the signal correlated PDF component, parametrized as a nonrelativistic Breit-Wigner function (green) and a Bifurcating Gaussian (green) for MC streams 1-5.

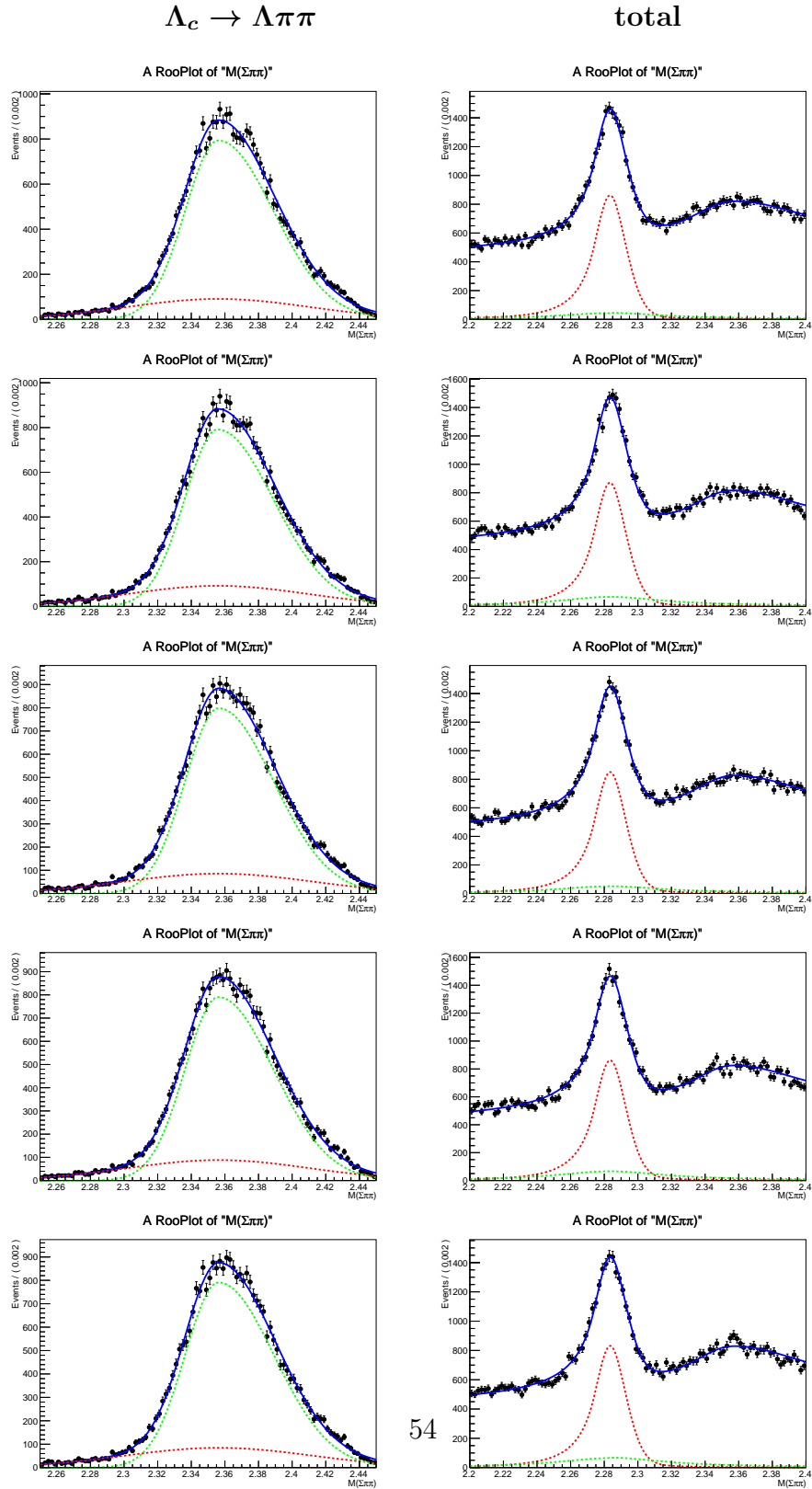


Figure 3.18: From upper left to lower right:  $\Lambda_c \rightarrow \Lambda \pi \pi$  parametrized as a bifurcating gaussian and a gaussian under variation of component streams. Total  $\Sigma^0 \pi^+ \pi^0$  PDFs for MC stream 1-5. The signal component is red, the signal correlated component is green and the background polynomial is yellow.

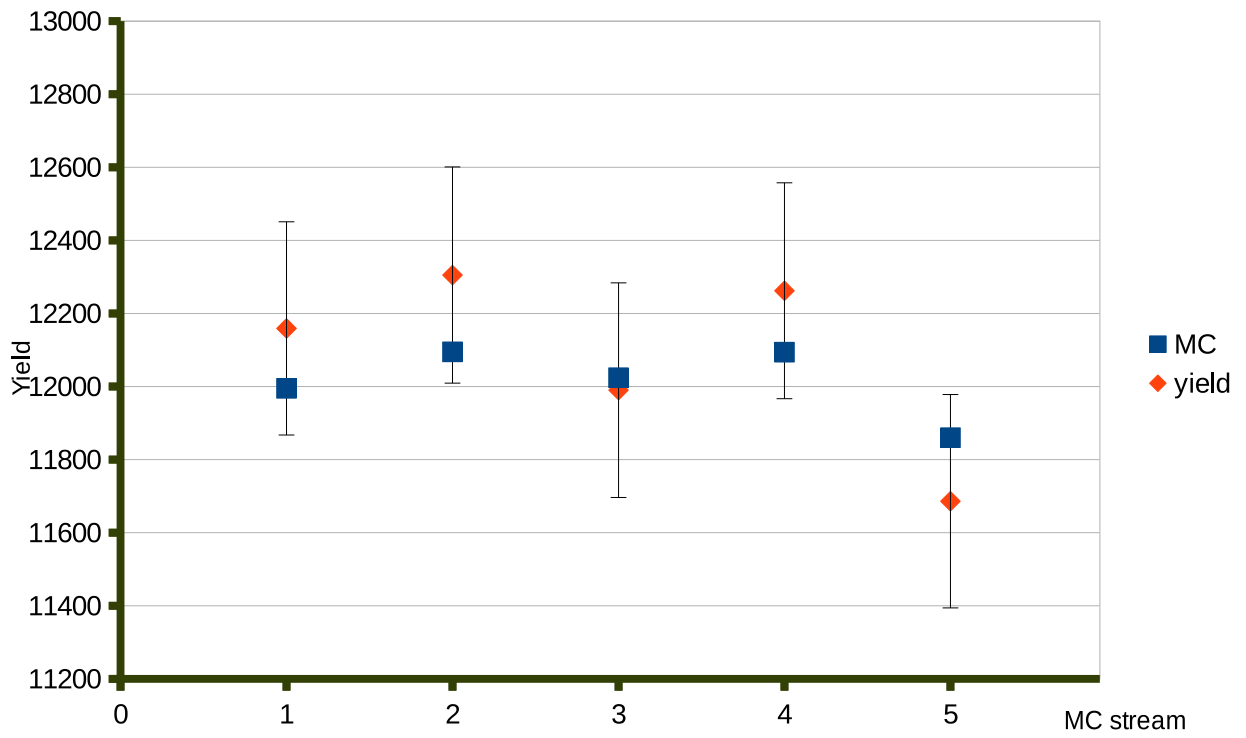


Figure 3.19: Yield for signal and correlated component with statistical error compared to MC truth.

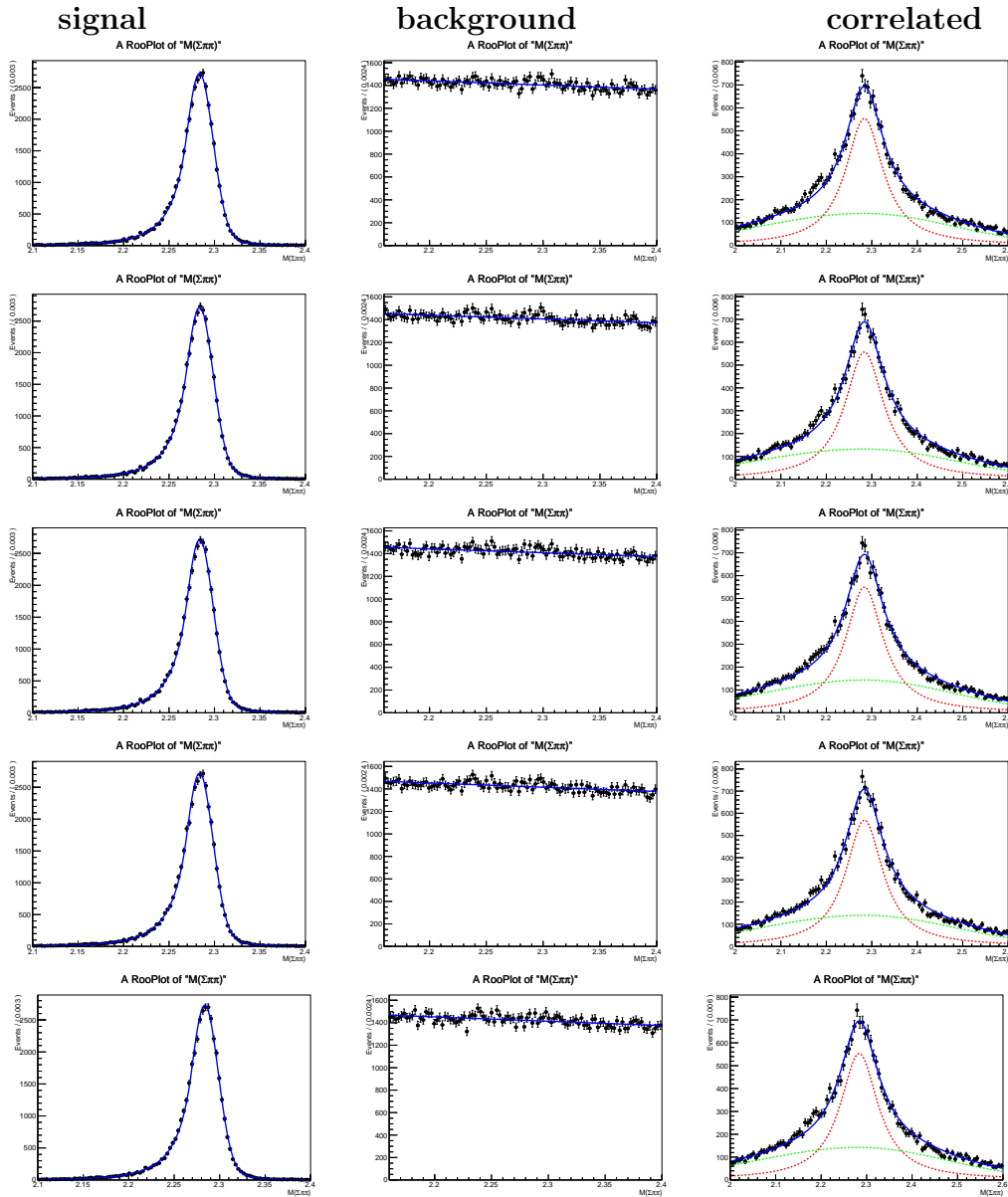


Figure 3.20:  $\Sigma^+\pi^0\pi^0$  PDFs. From top left to bottom right: Signal, parametrized as a Crystal Ball function (red) and a Gaussian (green), background parametrized as a Chebychev Polynomial of the order two and the signal correlated PDF component, parametrized as a nonrelativistic Breit-Wigner function (red) and a Bifurcating Gaussian (green) for MC streams 1-5 under variation of component streams.

total PDF

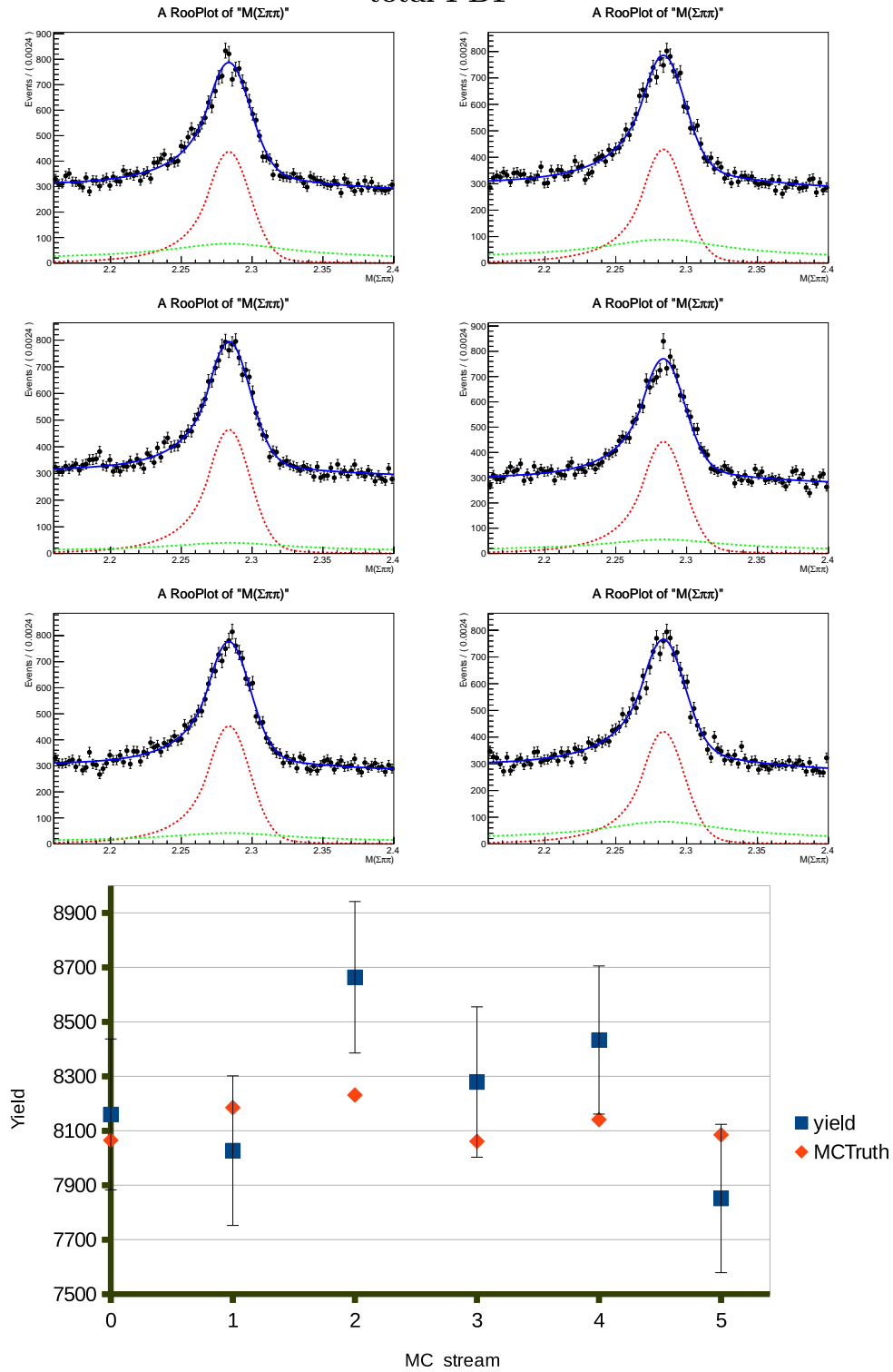


Figure 3.21: From upper left to lower right: Total  $\Sigma^+\pi^0\pi^0$  PDFs for MC stream 0-5. The signal component is red, the signal correlated component is green and the background polynomial is yellow. Yield for signal and correlated component with statistical error compared to MC truth.

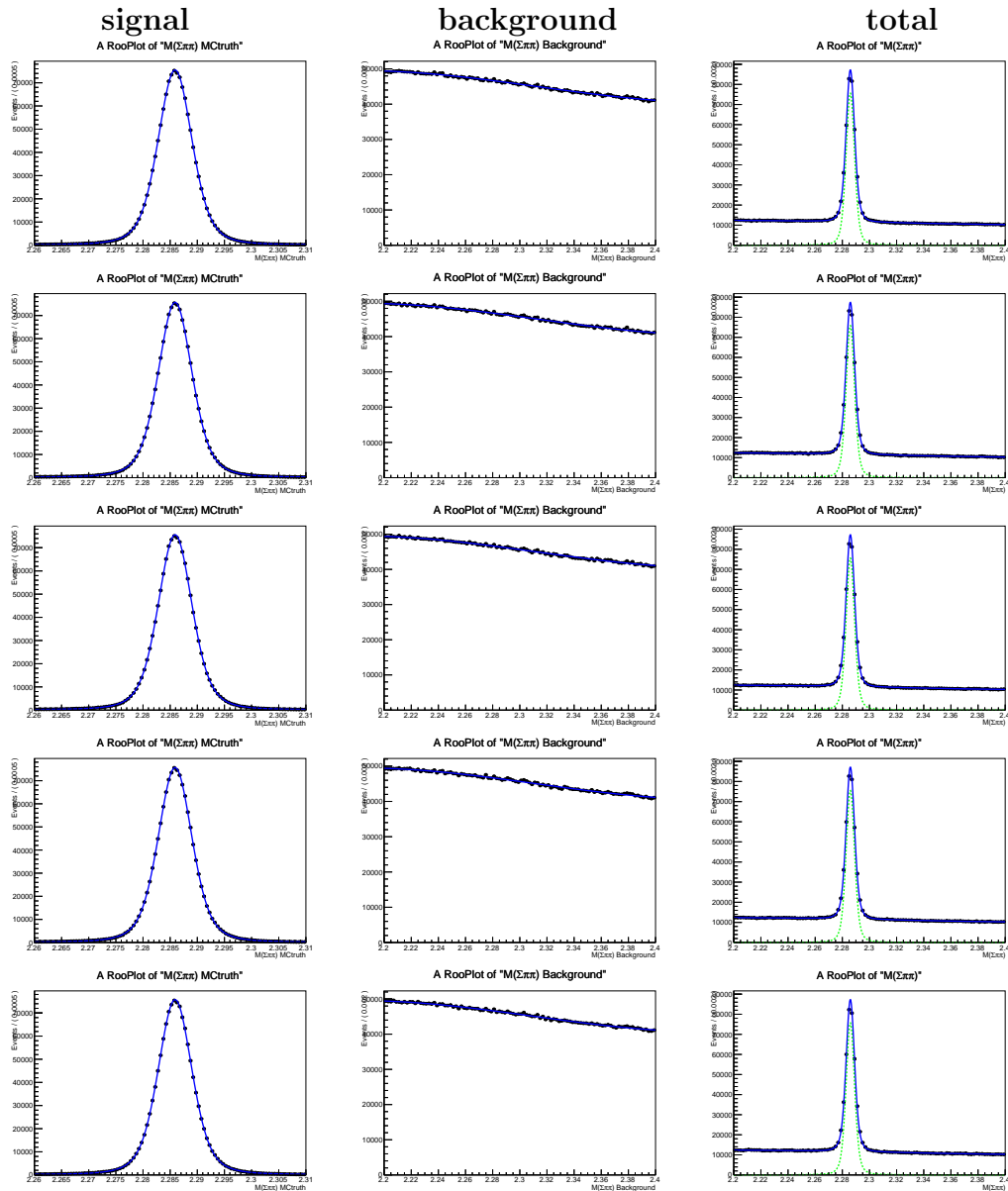


Figure 3.22:  $pK^-\pi^+$  PDFs. From top left to lower right: Signal, parametrized as two Gaussians and a Breit-Wigner function, background parametrized as a Chebychev Polynomial of the order three and total PDFs with signal (green) and background for MC stream 1 - 5. To determine parameters four of five MC streams are used. The total PDF is plotted for the remaining stream.

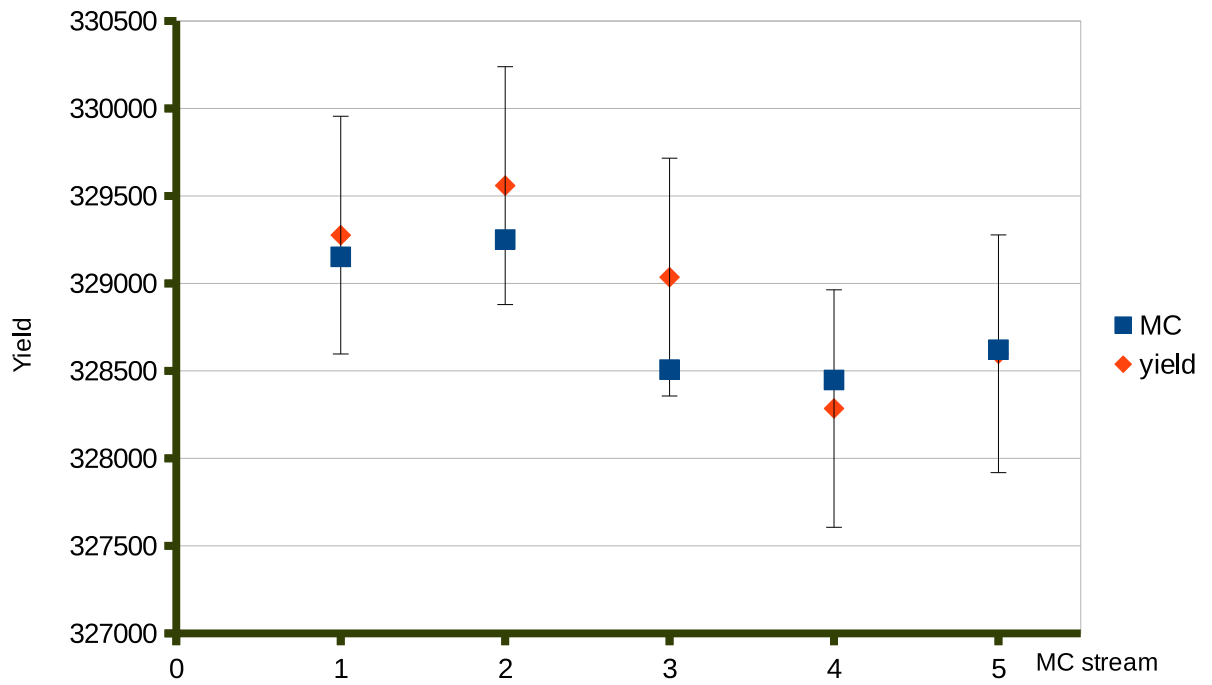


Figure 3.23: Yield for signal with statistical error compared to MC truth for the  $pK^-\pi^+$  channel.

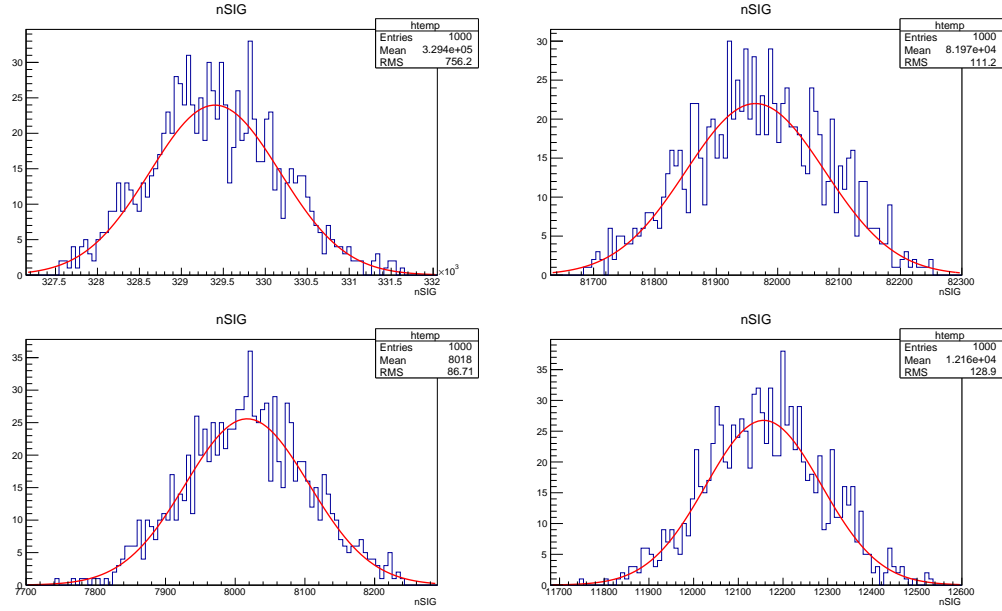


Figure 3.24: Fitted yield for toy MC study of  $pK^- \pi^+$ ,  $\Sigma^+ \pi^- \pi^+$ ,  $\Sigma^+ \pi^- \pi^0$  and  $\Sigma^+ \pi^0 \pi^0$

### 3.6 Systematic Uncertainties

In this chapter an estimation of systematic uncertainties for the measurement of branching ratios is given. One stream of MC is used as pseudo real data. Contributions that have no bearing on  $\mathcal{B}(\Sigma\pi\pi)/\mathcal{B}(pK^-\pi^+)$  are disregarded. Errors are listed in table 3.5

**PDF** parametrization is accounted for by repeating the fit a 1000 times while randomly drawing a value for parameters within their uncertainty. The fitted yield is plotted in Fig. 3.24. The width of the Gaussian distribution is taken as a systematic error.

**PID** corrections are determined for  $\mathcal{L}(K/\pi)$  and  $\mathcal{L}(\pi/K)$  using the correction tables supplied by the PID group [41]. The systematic error is averaged, the statistic error is summed up quadratically and a constant factor for run dependence is added. Proton ID corrections are determined for each event from the relevant table [40] and then summed quadratically. Conservatively it is assumed, that the errors in PID are uncorrelated.

$\pi^0$  reconstruction accounts for 1.45 % per  $\pi^0$  according to ref. [39]

**Fit stability** is tested by varying the fit limits for yield extraction by  $\pm 20$  MeV. The results can be found in Fig. 3.26. The yield difference for  $\pm 10$  MeV is taken as a systematic error.

**Other contributions** The fit for the yield of  $\Sigma^+\pi^0\pi^0$  is repeated with twice the contribution of  $\Lambda\rho^+$ . This changes signal yield by 0.75%. Since the parametrization of the  $\Sigma^+\pi^+\pi^-$  channel leads to a bias, it is added to the systematic error.

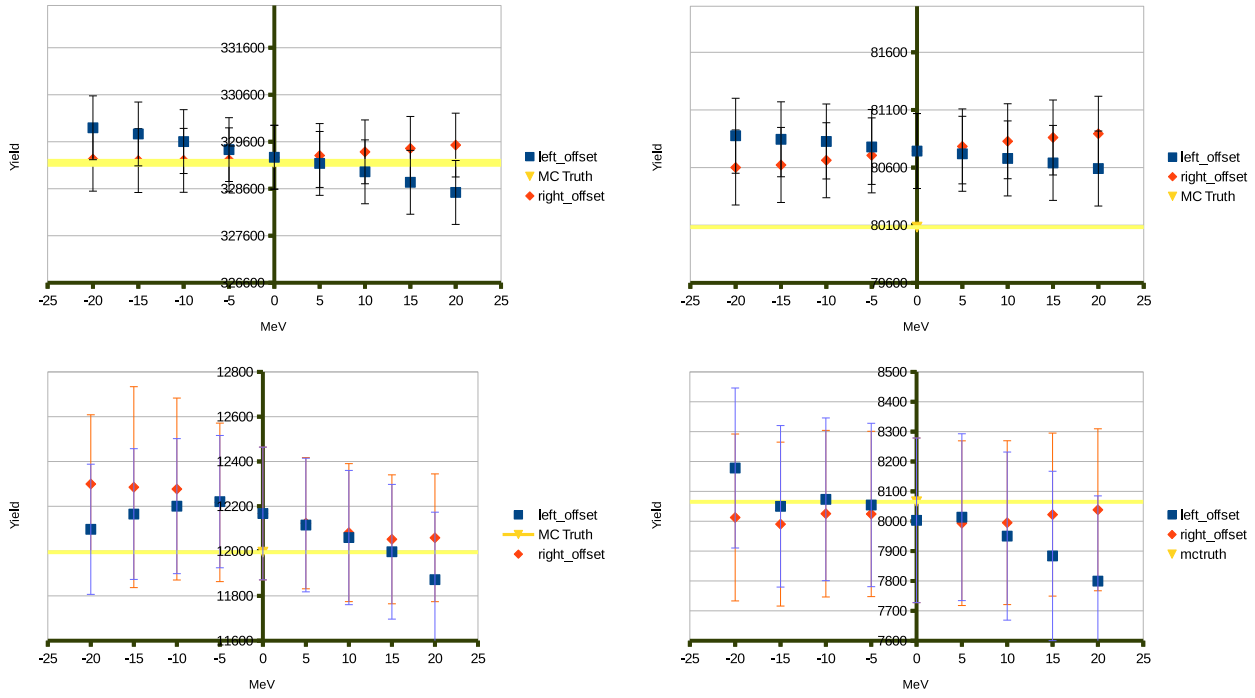


Figure 3.25: Fitted yield under range variation of  $pK^- \pi^+$ ,  $\Sigma^+ \pi^- \pi^+$ ,  $\Sigma^+ \pi^- \pi^0$  and  $\Sigma^+ \pi^0 \pi^0$

### 3.7 Branching ratios

The relative branching ratios are calculated according to

$$\frac{\mathcal{B}(\Sigma\pi\pi)}{\mathcal{B}(pK^-\pi^+)} = \frac{Y_{\Sigma\pi\pi}\epsilon_{pK^-\pi^+}}{Y_{pK^-\pi^+}\epsilon_{\Sigma\pi\pi}} \quad (3.4)$$

Where  $\epsilon$  stands for the reconstruction efficiency and  $Y$  for the yield. Results are given in table 3.4

Table 3.4: Reconstruction efficiency, and relative branching ratios  $\mathcal{B}$  with statistical and systematic error.

|                      | efficiency | $\mathcal{B}$              |
|----------------------|------------|----------------------------|
| $pK^-\pi^+$          | 5.61%      | 1                          |
| $\Sigma^+\pi^-\pi^+$ | 1.79%      | $0.72 \pm 0.003 \pm 0.025$ |
| $\Sigma^0\pi^+\pi^0$ | 0.56 %     | $0.36 \pm 0.012 \pm 0.008$ |
| $\Sigma^+\pi^0\pi^0$ | 0.38 %     | $0.36 \pm 0.0086 \pm 0.01$ |

### 3.8 $\Sigma\pi$ mass spectrum

The  $\Sigma\pi$  spectrum obtained from this analysis. The top Fig. is the total spectrum including background. The bottom is the background subtracted spectrum, overlaid with the theoretical prediction from [24] assuming several different scattering lengths. Please note that in the MC data there is no cusp effect since such an effect wasn't considered.

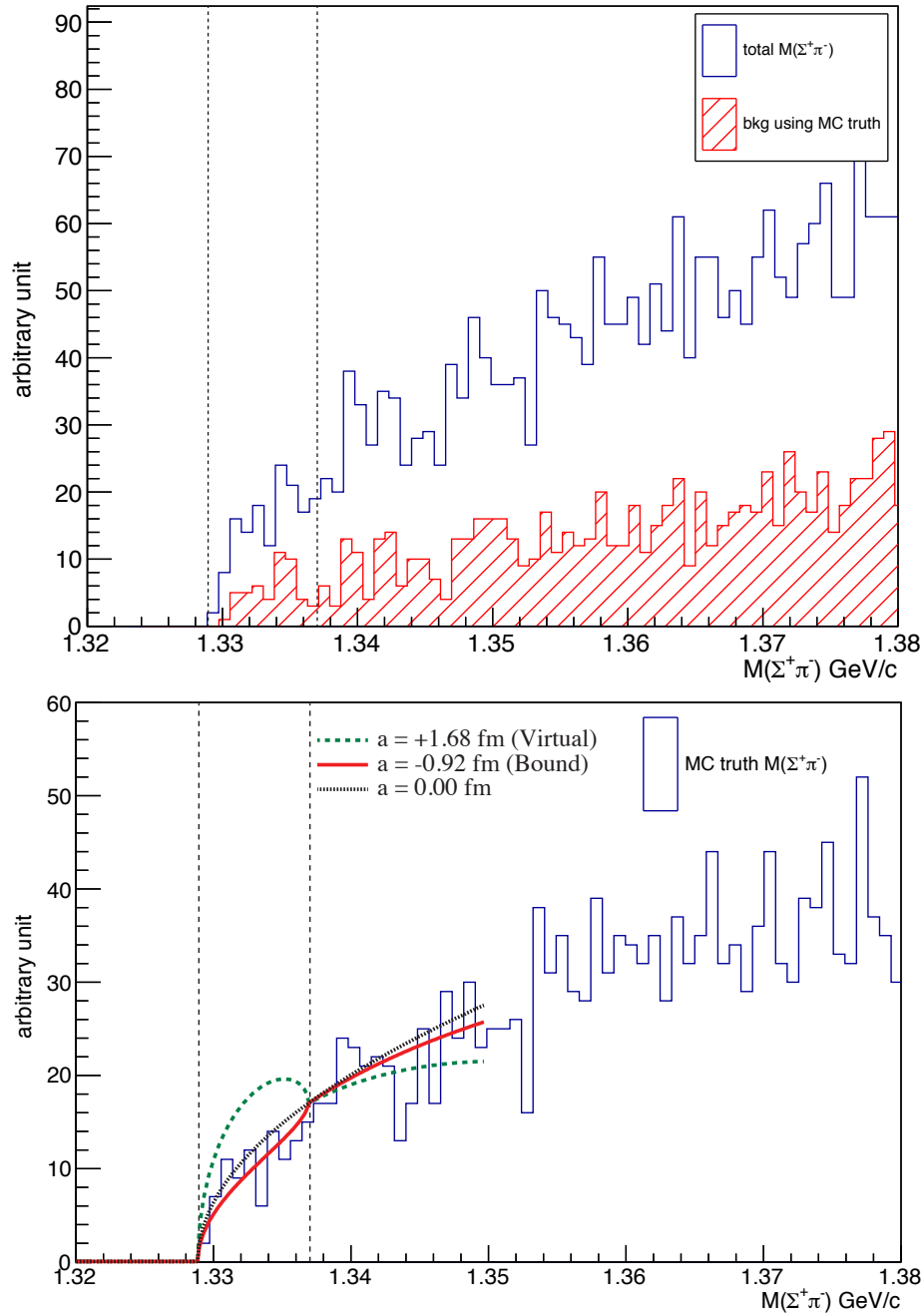


Figure 3.26: Top:  $\Sigma^+\pi^-$  invariant mass spectrum including background. Bottom:  $\Sigma^+\pi^-$  invariant mass spectrum overlaid with theoretical prediction [24] for the threshold cusp effect. The dotted line indicate the position of the thresholds for the higher and lower energy  $\Sigma\pi$  combination

|                          | $\mathcal{B}(\Sigma^+\pi^+\pi^-)$ | $\mathcal{B}(\Sigma^+\pi^0\pi^0)$ | $\mathcal{B}(\Sigma^0\pi^+\pi^-)$ |
|--------------------------|-----------------------------------|-----------------------------------|-----------------------------------|
| statistics(fit)          | 0.456                             | 3.404                             | 2.409                             |
| Pdf (parameter)          | 0.141                             | 1.084                             | 1.077                             |
| PID [%]                  |                                   |                                   |                                   |
| prot                     | 0.024                             | 0.023                             | 0.079                             |
| $p\text{-}pK^-\pi^+$     | 0.084                             | 0.084                             | 0.084                             |
| $K\pi$                   | 1.02                              | 1.02                              | 1.02                              |
| $\pi K$                  | 3.041                             | 0                                 | 1.538                             |
| $\pi K\text{-}pK^-\pi^+$ | 1.063                             | 1.063                             | 1.063                             |
| tracking                 | 0                                 | 0.7                               | 0                                 |
| $\pi^0$                  | 1.45                              | 2.5                               | 1.45                              |
| Fitstability             | 0.14                              | 1.01                              | 1.4                               |
| bias                     | 0.7                               | 0                                 | 0                                 |
| total syst               | 3.75                              | 3.4                               | 3.1                               |

Table 3.5: Table of systematic error contributions in percent

# Chapter 4

## Conclusion and Outlook

The purpose of this analysis is the determination of the  $\Sigma$ - $\pi$  scattering length. This thesis covers the blind MC studies conducted to develop a procedure for the extraction of the cusp effect from the  $\Sigma\pi$  invariant mass spectrum of the weak  $\Lambda_c \rightarrow \Sigma\pi\pi$  decays. This cusp effect reflects the scattering length. In accomplishing this goal high reconstruction efficiency and purity for  $\Lambda_c$  are essential. The optimized selection criteria obtained in this analysis can be used to determine the branching fraction of  $\Lambda_c \rightarrow \Sigma^+\pi^0\pi^0$  for the first time and to measure the branching fractions for  $\Sigma^+\pi^+\pi^-$  and  $\Sigma^0\pi^+\pi^0$  with higher precision. The selection and parametrization of probability density functions for yield extraction and a study of systematic errors on the determination of the branching fraction obtained by this procedure have been presented.

After approval by the internal review committee the analysis code can be run using real data. With this the measurement of the branching fractions should be concluded. Since the size of the threshold cusp effect is entirely unknown no statement about the precision of the scattering lengths obtained by this analysis can be made. In case of a small effect the statistical limitations an exact measurement using the procedure developed in this thesis will only be possible in a later experiment *e.g.* Belle II or possibly PANDA.

# Chapter 5

## Apendix

### 5.1 Tables of fit parameters

Table 5.1: Fit Parameters for streams 0-2 of the  $\Sigma^+\pi^+\pi^-$  decay channel

|                    | parameter          | str1       |           | str2       |           |
|--------------------|--------------------|------------|-----------|------------|-----------|
|                    |                    |            | error     |            | error     |
| signal +correlated | fsig (gauss/bigau) | 0.54331    | 0.00514   | 0.54133    | 0.0051494 |
|                    | meansig            | 2.286      | 8.07E-006 | 2.286      | 8.07E-006 |
|                    | sigmabwig          | 0.0071569  | 8.65E-005 | 0.0071617  | 8.63E-005 |
|                    | sigmagau           | 0.003933   | 1.97E-005 | 0.0039277  | 1.97E-005 |
| bkg                | coef1              | -5.25E-002 | 2.41E-003 | -0.0534311 | 0.0024115 |
|                    | coef2              | -2.35E-002 | 2.36E-003 | -0.0250803 | 0.0023575 |
| total              | yield signal +cor  | 80725      | 325.22    | 79977      | 323.88    |
|                    | yield background   | 129128     | 392.64    | 128520     | 391.71    |

Table 5.2: Fit Parameters for streams 3-25 of the  $\Sigma^+\pi^+\pi^-$  decay channel

| str3       |           | str4       |           | str5       |           |
|------------|-----------|------------|-----------|------------|-----------|
|            | error     |            | error     |            | error     |
| 0.53978    | 0.0051382 | 0.54112    | 0.0051382 | 0.53787    | 0.0050568 |
| 2.286      | 8.07E-006 | 2.286      | 8.07E-006 | 2.286      | 8.09E-006 |
| 0.0071498  | 8.57E-005 | 0.0071434  | 8.59E-005 | 0.0071009  | 8.33E-005 |
| 0.0039321  | 1.98E-005 | 0.0039291  | 1.98E-005 | 0.0039516  | 1.99E-005 |
| -0.0547278 | 0.0024109 | -0.0515244 | 0.0024141 | -0.0534413 | 0.0024107 |
| -0.0241208 | 0.0023568 | -0.0254356 | 0.0023612 | -0.0232087 | 0.0023552 |
| 80327      | 324.47    | 80821      | 325.41    | 81095      | 325.56    |
| 127921     | 390.99    | 129263     | 392.85    | 127709     | 390.64    |

Table 5.3: Fit Parameters for streams 0-2 of the  $\Sigma^0\pi^+\pi^0$  decay channel

|            | parameter         | str1       |            | str2      |            |
|------------|-------------------|------------|------------|-----------|------------|
|            |                   |            | error      |           | error      |
| signal     | fsig (bwign/cb)   | 0.77405    | 0.013556   | 0.77121   | 0.013639   |
|            | meansig           | 2.2834     | 8.35E-005  | 2.2834    | 8.33E-005  |
|            | sigmagbwign       | 0.018493   | 0.0011705  | 0.018481  | 0.0011617  |
|            | sigmacb           | 0.0097937  | 0.00013243 | 0.0098503 | 0.00013305 |
|            | a                 | 0.97869    | 0.026949   | 0.99143   | 0.027361   |
|            | n                 | 3.8636     | 0.24737    | 3.7946    | 0.24265    |
| signalcorr | fbwign/bigau      | 0.94548    | 0.0049303  | 0.94073   | 0.0072786  |
|            | sigmabwign_sigcor | 0.078443   | 0.001136   | 0.078886  | 0.0011402  |
|            | sigmal_cor        | 0.00011179 | 0.00020192 | 0.016495  | 0.0079792  |
|            | sigmar_cor        | 0.73272    | 0.37386    | 0.68116   | 2.3121     |
| bkg        | Coef 1            | 0.12384    | 0.0037023  | 0.12278   | 0.0036932  |
| lampipi    | fraction          | 0.18059    | 0.015018   | 0.18183   | 0.014978   |
|            | meanlampipi       | 2.3561     | 0.00058165 | 2.3558    | 0.00057327 |
|            | sigmal            | 0.019761   | 0.00054958 | 0.019727  | 0.00054104 |
|            | sigmar            | 0.032813   | 0.00047224 | 0.033008  | 0.00046986 |
|            | sigmal            | 0.054304   | 0.0028833  | 0.053647  | 0.002769   |

Table 5.4: Fit Parameters for streams 3-5 of the  $\Sigma^0\pi^+\pi^0$  decay channel

| str3      |            | str4      |            | str5       |            |
|-----------|------------|-----------|------------|------------|------------|
|           | error      |           | error      |            | error      |
| 0.7787    | 0.014063   | 0.77901   | 0.014892   | 0.77336    | 0.013818   |
| 2.2835    | 8.39E-005  | 2.2835    | 8.76E-005  | 2.2835     | 8.36E-005  |
| 0.018898  | 0.0012704  | 0.019975  | 0.0014282  | 0.018661   | 0.0012007  |
| 0.0096887 | 0.0001303  | 0.0096615 | 0.00013192 | 0.0096673  | 0.00013104 |
| 0.96059   | 0.026348   | 0.95163   | 0.027437   | 0.95178    | 0.026083   |
| 4.0552    | 0.26309    | 4.1952    | 0.28535    | 4.066      | 0.26346    |
| 0.92639   | 0.0095074  | 0.92753   | 0.0096627  | 0.94179    | 0.0049072  |
| 0.077863  | 0.0013153  | 0.078422  | 0.0013449  | 0.077177   | 0.0011248  |
| 0.039835  | 0.01199    | 0.040256  | 0.012999   | 0.00069539 | 0.0011185  |
| 0.55041   | 0.075589   | 3.2       | 2.3997     | 3.7398     | 2.501      |
| 0.0037032 | 0.0037032  | 0.12351   | 0.0036955  | 0.12298    | 0.0036982  |
| 0.17309   | 0.015177   | 0.17683   | 0.014813   | 0.17244    | 0.015175   |
| 2.3563    | 0.00057989 | 2.3561    | 0.00057813 | 2.3563     | 0.00058417 |
| 0.020024  | 0.00055025 | 0.019923  | 0.00053382 | 0.020036   | 0.00055616 |
| 0.032662  | 0.00046075 | 0.03269   | 0.00046824 | 0.03297    | 0.00046451 |
| 0.055274  | 0.0031362  | 0.054109  | 0.0028607  | 0.055739   | 0.0032316  |

Table 5.5: Fit Parameters for streams 0-3 of the  $\Sigma^+\pi^0\pi^0$  decay channel

|        | parameter   | str0       |            | str1       |           | str2       |           |
|--------|-------------|------------|------------|------------|-----------|------------|-----------|
|        |             |            | error      |            | error     |            | error     |
| signal | gauss/cb    | 0.93745    | 0.0055149  | 0.93597    | 0.0055741 | 0.9372     | 0.0054638 |
|        | meansig     | 2.2836     | 0.00014472 | 2.2837     | 1.46E-004 | 2.2837     | 1.51E-004 |
|        | sigmacb     | 0.014853   | 0.00014897 | 0.014831   | 1.51E-004 | 0.0148     | 1.54E-004 |
|        | sigmagauss  | 0.044705   | 0.002001   | 0.044753   | 0.0019964 | 0.044766   | 0.0020079 |
|        | a           | 0.98697    | 0.022825   | 0.97847    | 0.022907  | 0.9757     | 0.023614  |
|        | n           | 3.8291     | 0.19208    | 3.968      | 0.20482   | 3.8983     | 0.20052   |
| cor    | bwign/bigau | 0.55775    | 0.025626   | 0.57525    | 0.026006  | 0.55172    | 0.025278  |
|        | sigmabwign  | 0.10114    | 0.0043748  | 0.10384    | 0.0044015 | 0.10063    | 0.0043321 |
|        | sigmal      | 0.22776    | 0.013352   | 0.24053    | 0.016488  | 0.22258    | 0.012199  |
|        | sigmar      | 0.19535    | 0.0072386  | 0.20071    | 0.0081813 | 0.19388    | 0.0069263 |
| bkg    | Coef 1      | -0.0310709 | 0.0046192  | -0.0289546 | 0.0046163 | -2.90E-002 | 0.0046187 |
| yield  | signal      | 8159.9     | 277.26     | 8026.8     | 274.6     | 8663.6     | 278.08    |
|        | signal cor  | 4756.3     | 1095.6     | 5600.4     | 1077.5    | 2516.1     | 1099.4    |
|        | background  | 27455      | 894.24     | 26672      | 878.85    | 29053      | 900.22    |

Table 5.6: Fit Parameters for streams 3-5 of the  $\Sigma^+\pi^0\pi^0$  decay channel

| str3     |            | str4     |            | str5       |           |
|----------|------------|----------|------------|------------|-----------|
|          | error      |          | error      |            | error     |
| 0.93088  | 0.0057813  | 0.93064  | 0.0060727  | 0.93592    | 0.0055576 |
| 2.2836   | 1.55E-004  | 2.2836   | 1.51E-004  | 2.2836     | 1.50E-004 |
| 0.014753 | 1.59E-004  | 0.014768 | 1.58E-004  | 0.014823   | 1.54E-004 |
| 0.043467 | 0.0018064  | 0.041874 | 0.0017004  | 0.044432   | 0.0019627 |
| 0.96719  | 0.024304   | 0.98937  | 0.024489   | 0.98426    | 0.023811  |
| 3.9599   | 0.20952    | 3.8222   | 0.1962     | 3.8532     | 0.19803   |
| 0.93088  | 0.0057813  | 0.93064  | 0.0060727  | 0.55625    | 0.025627  |
| 2.2836   | 0.0001552  | 2.2836   | 0.00015125 | 0.10099    | 0.0043744 |
| 0.014753 | 0.00015857 | 0.014768 | 0.00015761 | 0.22535    | 0.012858  |
| 0.043467 | 0.0018064  | 0.041874 | 0.0017004  | 0.19328    | 0.0069476 |
| 0.96719  | 0.024304   | 0.98937  | 0.024489   | -3.23E-002 | 4.61E-003 |
| 8278.8   | 276.13     | 8433.1   | 271.93     | 7851.1     | 272.53    |
| 3440.1   | 1064       | 2628.7   | 1073       | 5211.2     | 1075.2    |
| 27273    | 864.15     | 28261    | 879.04     | 26236      | 877.19    |

 Table 5.7: Fit Parameters for streams 0-2 of the  $pK^-\pi^+$  decay channel

|        | parameter | str1        |             | str2       |             |
|--------|-----------|-------------|-------------|------------|-------------|
|        |           |             | error       |            | error       |
| signal | meansig   | 2.2859      | 3.28E-006   | 2.2859     | 3.28E-006   |
|        | fsig      | 0.59832     | 1.11E-002   | 0.60326    | 1.12E-002   |
|        | fsig2     | 0.16888     | 1.40E-002   | 0.15975    | 1.39E-002   |
|        | sigmagau  | 0.0029895   | 0.000029841 | 0.003012   | 0.000031393 |
|        | sigmagau2 | 0.0051481   | 0.00011904  | 0.0052746  | 0.00013525  |
|        | sigmabwig | 0.0069138   | 0.00018982  | 0.0066729  | 0.00017817  |
| bkg    | coef1     | -0.0971717  | 0.00093268  | -9.68E-002 | 9.33E-004   |
|        | coef2     | -0.00463653 | 0.00078797  | -4.70E-003 | 7.88E-004   |
|        | coef3     | 0.0058459   | 0.0007753   | 6.15E-003  | 7.75E-004   |
| total  | numsig    | 329276      | 679.58      | 329559     | 679.79      |
|        | numbkg    | 1.14E+006   | 1126.8      | 1.14E+006  | 1127.5      |

Table 5.8: Fit Parameters for streams 3-5 of the  $pK^- \pi^+$  decay channel

| str3        |             | str4        |             | str5       |             |
|-------------|-------------|-------------|-------------|------------|-------------|
|             | error       |             | error       |            | error       |
| 2.2859      | 3.28E-006   | 2.2859      | 3.29E-006   | 2.2859     | 3.29E-006   |
| 0.58942     | 1.15E-002   | 0.59729     | 8.59E-003   | 0.59523    | 8.79E-003   |
| 0.17375     | 1.41E-002   | 0.16461     | 1.04E-002   | 0.16665    | 1.07E-002   |
| 0.0029855   | 0.000029913 | 0.0030012   | 0.000024117 | 0.002994   | 0.000024695 |
| 0.005097    | 0.00011402  | 0.0051875   | 0.000093368 | 0.005174   | 0.000094417 |
| 0.006827    | 0.00017641  | 0.0067368   | 0.00016683  | 0.006723   | 0.00016809  |
| -0.097353   | 0.00093286  | -0.0966729  | 0.00093263  | -0.0969364 | 0.00093283  |
| -0.00436846 | 0.00078798  | -0.00436307 | 0.00078771  | -0.0036592 | 0.00078759  |
| 0.0060538   | 0.00077542  | 0.0062278   | 0.00077531  | 0.0061306  | 0.00077523  |
| 329036      | 679.56      | 328285      | 678.71      | 328598     | 679.36      |
| 1.14E+006   | 1127.6      | 1.14E+006   | 1126.3      | 1.14E+006  | 1127.3      |

# Bibliography

- [1] Y. Akaishi and T. Yamazaki, Phys. Rev. C 65 (2002) 044005.
- [2] T. Hyodo and W. Weise, Phys. Rev. C 77 (2008) 35204.
- [3] Y. Ikeda, T. Hyodo and W. Weise Phys. Lett. B 706 (2011) 63.
- [4] A. Doté, H. Horiuchi, Y. Akaishi, T. Yamazaki, Phys. Lett. B 590 (2004) 51.
- [5] S. Wycech, A.M. Green, Phys. Rev. C 79 (2009) 14001.
- [6] A. Doté, T. Hyodo and W. Weise, Phys. Rev. C 79 (2009) 14003.
- [7] M. Agnello *et al.*, Phys. Rev. Lett. 94 212303 (2005).
- [8] T. Yamazaki *et al.*, Phys. Rev. Lett. 104 132502 (2010).
- [9] P. Kienle *et al.*, Eur. Phys. J. A 48 183 (2012).
- [10] K. Suzuki *et al.*, Nucl. Phys. A 827, 312C (2009).
- [11] Y. Ichikawa *et al.*, .Progr. of Theo. and Exp. Phys., (2015) 21D01.
- [12] M. Bazzi *et al.*, Phys. Lett. B 704 (2011) 113.
- [13] G.S. Abrams, B. Sechi-Zorn, Phys. Rev. 139 (1965) B454; M. Sakitt, *et al.* , Phys. Rev. 139 (1965) B719; J.K. Kim, Phys. Rev. Lett. 14 (1965) 29; M. Csejthey-Barth, et al., Phys. Lett. 16 (1965) 89; T.S. Mast, et al., Phys. Rev. D 14 (1976) 13; R.O. Bangerter, *et al.*, Phys. Rev. D 23 (1981) 1484; J. Ciborowski, et al., J. Phys. G 8 (1982) 13; D. Evans, et al., J. Phys. G 9 (1983) 885.
- [14] Y. Ikeda, T. Hyodo, D. Jido, H. Kamano, T. Sato, K. Yazaki, Progress of Theo. Phys., 125 (2011) 1205.
- [15] T. Hyodo and D. Jido, Prog. Part. Nucl. Phys. 67 55 (2012).

- [16] R.H. Dalitz, S.F. Tuan, Phys. Rev. Lett. 2 (1959) 425.; R.H. Dalitz, S.F. Tuan, Ann. Phys. 10 (1960) 307.
- [17] J. M. M. Hall *et al.*, arXiv:1411.3402v1.
- [18] D. Jido, J.A. Oller, E. Oset, A. Ramos, U.-G. Meißner, Nucl. Phys. A 725 (2003) 181.
- [19] J. Gasser, PoS(EFT09) 029.
- [20] P. Budini and L. Fonda, Phys. Rev. Lett. 6(8) (1961) 419.
- [21] N. Cabibbo, 93 (2004) 121801.
- [22] J.R. Batley, C. Lazzeroni, D. Munday *et al.* Phys. Lett. B 633 (2006) 173?182.
- [23] J.R. Batley, A.J. Culling, G. Kalmus, Eur. Phys. J. C 64 (2009) 589.
- [24] T. Hyodo and M. Oka, Phys. Rev. C84, 035201 (2011).
- [25] K.A. Olive *et al.* (Particle Data Group), Chin. Phys. C, 38, 090001 (2014).
- [26] C. Schwanda Habilitationsschrift (2012).
- [27] J. Beringer *et al.* [Particle Data Group Collaboration], Phys. Rev. D **86** (2012) 010001.
- [28] N. Cabibbo, Phys. Rev. Lett. **10**, (1963) 531;  
M. Kobayashi and T. Maskawa, Prog. Theor. Phys. **49**, (1973) 652.
- [29] K. Abe *et al.* [Belle Collaboration], Phys. Rev. Lett. **87**, (2001) 091802. [arXiv:hep-ex/0107061].
- [30] B. Aubert *et al.* [BABAR Collaboration], Phys. Rev. Lett. **87**, (2001) 091801. [arXiv:hep-ex/0107013].
- [31] J. Charles *et al.* [CKMfitter Group], Eur. Phys. J. C **41**, 1 (2005) [arXiv:hep-ph/0406184]; and web updates of the numerical results.
- [32] Y. Amhis *et al.* [Heavy Flavor Averaging Group Collaboration], arXiv:1207.1158 [hep-ex].
- [33] S. Kurokawa and E. Kikutani, Nucl. Instrum. Meth. A **499**, (2003) 1, and other papers included in this volume.

- [34] A. Abashian *et al.* [Belle Collaboration], Nucl. Instrum. Meth. A **479** (2002) 117.
- [35] D. J. Lange, Nucl. Instrum. Meth. A **462** (2001) 152.
- [36] R. Brun *et al.*, GEANT 3.21, CERN Report DD/EE/84-1, 1984.
- [37] A. Sibidanov and K.E.Varvel, Belle Note 1206.
- [38] J. Yelton, Belle Note 1380 (2015).
- [39] S. Ryu, Belle Note 1224 (2012).
- [40] K. Tien, M. Wang, Belle Note 1279 (2012).
- [41] S. Nishida, Belle Note 779 (2015).